Investigation on Modified Zinc Oxide for Ferroelectric and Optical Applications

Thesis submitted towards the partial fulfillment of the requirements for the award of the degree of

Master of Technology
in
Materials & Metallurgical Engineering

Submitted by

ISHAN CHOUDHARY

ROLL. No. 600802008

Under the supervision of

Dr. K.K. RAINA

Deputy Director & Distinguished Professor (SPMS)

Thapar University, Patiala

School of Physics and Material Science

THAPAR UNIVERSITY,

PATIALA – 147004,

INDIA

July, 2010

BONAFIDE CERTIFICATE

I hereby declare that the work which is being presented in the thesis entitled ***"Investigation on modified ZnO for ferroelectric and optical applications"*** is an authentic record of my own work carried out as requirement for the award of the degree of M.Tech in Material science and Metallurgical Engineering at Thapar Institute of Engineering and Technology (Deemed University) Patiala, under the guidance of **Dr. K.K.Raina, Deputy Director & Distinguished Professor, School of Physics and Material Science and Engineering** during January to July 2010.

It is to certify that the above statement made by the candidate is correct and true to the best of my knowledge

(Dr. K.K.Raina)

Deputy Director & Distinguished Professor (SPMS)

Thapar University, Patiala

Countersigned by:

2/7/10

Dr. O.P. Pandey

Prof. & Head (SPMS)

Thapar University, Patiala

23/7/10

Dr. R.K. Sharma

Dean Academic Affairs

Thapar University, Patiala

AKNOWLEDGEMENT

It takes a lot of hard work and austere discipline to really make the things happening. I am indebted to all the people who provided the assistance, encouragement and cooperation to complete my work.

I would like to express my sincere gratitude to my esteemed and worthy supervisor **Dr. K.K.Raina, Deputy Director Thapar university & Distinguished Professor, School of Physics and Materials Science,** *for his insight help, guidance, effective supervision and encouragement in carrying out this dream come true. His wide knowledge and his logical way of thinking have been of great value for me.*

I am deeply grateful to **Dr. O.P. Pandey, Professor & Head, School of Physics and Material Science** *for his detailed and constructive comments, and for his important support throughout this work. His ideas and concepts made a remarkable influence on my career in the field of material science.*

I warmly thank **Dr. Kulvir singh, Associate Professor, School of Physics and Material Science** *for their kind support, guidance and untiring help during my difficult moments.*

I have no words to express to my ***Parents*** *who always a constant inspiration for me and supporting me spiritually throughout my life.*

I wish my heartfelt thanks to research scholars **Shikha Kapila Ravi Shukla, Neeraj Sharma, Parveen Kumar, Renu Dahiya, Rekha Gandhi** *for their generous help and good wishes.*

I am also thankful to all the staff members of the School of Physics and Materials Science for their full cooperation, motivation

*and generous support. I would also like thanks to my friends **Sunita Mehta, Sumit Bhardwaj, and Pankaj Chamoli** who stand with me in every situation without them this work would not have been accomplished.*

*Above all I render my gratitude to the **ALMIGHTY** who bestowed self-confidence, ability and strength in me to complete this work.*

ISHAN CHOUDHARY

ABSTRACT

In this approach undoped and doped (Samarium, Europium, Titanium, Niobium) ZnO samples were prepared via chemical route (co-precipitation) in the basic medium by adjusting the pH about 10.82. Undoped and doped samples were examined by XRD, FTIR, UV-Visible Spectroscopy, Photoluminescence spectroscopy , LCR meter, P-E loop tracer and SEM to investigate the structural, chemical, optical, dielectric, ferroelectric, and morphological nature of the samples. The XRD pattern of doped sample showed that no impurity peaks appeared and no change in the wurtzite hexagonal structure of ZnO, which confirming that dopant ions successfully substitute the Zinc ions. Chemical analysis is in good agreement with the structural analysis as only one reflection (455.54 cm^{-1}) corresponding to Zn-O has been observed. Optical spectra infer that optical band gap decreased in doped ZnO in comparison to undoped. Photoluminescence investigation reveals the presence of green and blue colour emission in undoped and doped ZnO samples at 190 nm excitation wavelength; interestingly Europium doped system show orangish-yellow luminescence at 254 nm excitation wavelength. Temperature and frequency dependent dielectric measurements indicates transition at 71^0c for pure, 82^0c for 0.25 % and 157^0c for 1% Titanium doped ZnO, which reflects certain shift in T_c , which gives an idea about presence of ferroelectricity in these systems. P-E loops for the Ti (0.25 and 1%) doped ZnO systems were found to be lossy in nature. Morphological study does not give any significant inference; only clusters of spherical particles have been found.

CONTENTS

List of Figures

List of Tables

CHAPTER 1

INTRODUCTION

1.1) PREAMBLE:

Nanocrystalline semiconductors have been the subjects of numerous investigations in the past two decades. If the semiconductor particles become smaller the Bohr radius of the exciton, so called quantum size effect occur. [1-4] As a result of these quantum size effects, the band gap increases and at the edges of the valence and conduction band discrete energy levels occur. These quantum size effects have stimulated great interest in both basic and applied research. The wide band gap semiconductor ZnO is well known for its multifunctionality in the form of ferromagnetism, ferroelectricity, piezoelectricity, optical and gas sensors applications. ZnO nanostructures such as nanowires, nanotubes, nanobelts, nanosheets and nanorods are promising building blocks for optical and electronic devices because of the potential application in the field of blue-light emitting, short wavelengths laser diodes, solar cells, transparent and conducting electrode in solar cells, surface acoustic wave devices chemical and biological sensors.[5-7] The preference of ZnO has gained impetus during last few years because of the possibility of its relatively simple synthesis into nanoscale structures. Furthermore, functional devices such as nanostructure field-effect transistors (FETs), piezoelectric nanosensors and nanolasers have already been realized. [8-10]

Doping of the different elements in ZnO has a drastic effect on the properties for example:

a) Ferromagnetism in ZnO by Cobalt and Manganese.
b) Ferroelectricity in ZnO by Lithium and Vanadium.
c) Enhancement in the optical properties of ZnO by Magnesium and rare earth elements.
d) Increment in conductivity by Aluminum doping in ZnO thin films without impairing its optical transmission.
e) With suitable co-doping one may expect to form a *p-n* junction as well.

In the present work influence of the doping of different elements **(Samarium, Europium, Titanium and Niobium)** in the ZnO has been studied for the optical and ferroelectric properties. The dopants are chosen in such a way that they possess a higher charge and greater ionic size in comparison of Zinc.

1.2) BRIEF OVERVIEW OF ZnO CHARACTERISTICS:

Zinc oxide (ZnO) is a wide band gap (3.26 eV) often called as II-VI compound semiconductor because zinc and oxygen belong to the 2nd and 6th groups of the periodic table, respectively. Zinc oxide crystallizes in three forms:

a) Hexagonal wurtzite

b) Cubic zincblende, and

c) The rarely observed cubic rocksalt.

The wurtzite structure is most stable at ambient conditions and thus most common with lattice spacing a = 0.325 nm and c = 0.521 nm. [11] As shown below in Fig.1.1

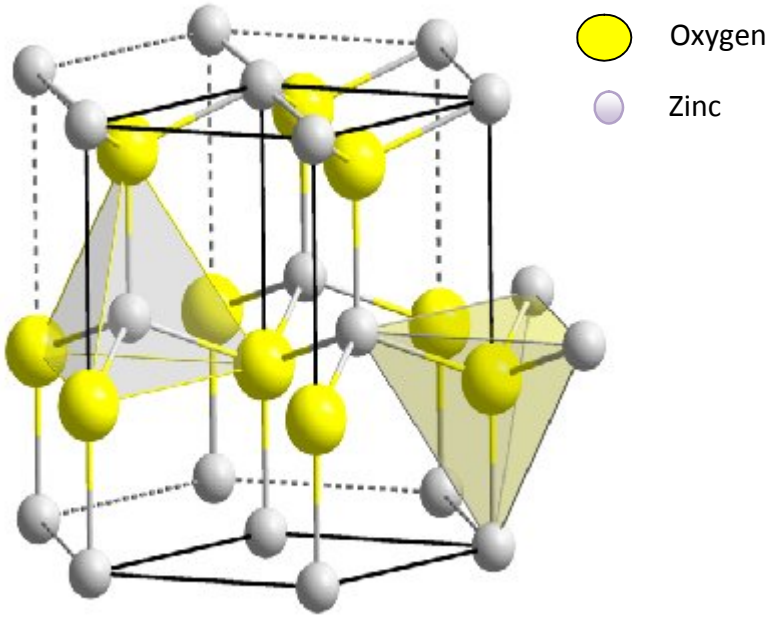

Fig.1.1 Wurtzite structure of ZnO

The zincblende form can be stabilized by growing ZnO on substrates with cubic lattice structure. In both cases, the zinc and oxide centers are tetrahedral. The rocksalt (NaCl-type) structure is only observed at relatively high pressures about 10 GPa. The bonding in ZnO is largely ionic, which explains its strong piezoelectricity. The basic characteristics of ZnO have been tabulated in Table 1.1.

Table1.1 Characteristics of ZnO

S.No	Property	Value
1	Density (g/cc)	5.606
2	Bond length (μm)	1.977
3	Melting point (^{0}c)	1975
4	Thermal conductivity	0.6 , 1-1.2
5	Static dielectric constant	8.656
6	Refractive index	2.008, 2.029
7	Energy gap (eV, direct)	3.26
8	Exciton binding energy (MeV)	60
9	Ionic character (%age)	62
10	Heat capacity Cp (cal/mol K)	9.6
11	Youngs modulus E (Gpa)	111.2±4.7

ZnO is a relatively soft material with approximate hardness of 4.5 on the Mohs scale. [12] Its elastic constants are smaller than those of relevant III-V semiconductors, such as GaN. The high heat capacity and heat conductivity, low thermal expansion and high melting temperature of ZnO are beneficial for ceramics. ZnO posses a direct band gap of 3.26 eV. Advantages associated with a large band gap include higher breakdown voltages, ability to sustain large electric fields, lower electronic noise, and high-temperature and high-power operation. The band gap of ZnO can further be tuned by doping with different elements which include Mg, Al, Mn, Co, Cu etc. and thus give rise to enhanced optical properties.

ZnO posse's n-type character even if there is no doping in it. This is mainly due to its non stoichiometry. The n-Type doping in the ZnO can be easily obtained by doping of Group III elements in pure ZnO which makes it suitable for the electronic applications. On the other hand p-Type doping in ZnO is quite difficult and cannot be easily achieved because of low solubility of p-type dopants. [13] Known p-type dopants include group-I elements Li, Na, K; group-V elements N, P and As; as well as copper and silver. Current limitations to p-doping do not limit electronic and optoelectronic applications of ZnO, which usually require junctions of n-type and

p-type material. As such ZnO posses many applications which include Piezoelectric sensing, Gas sensing, Magnetic sensing and in optics. The present work was to study the optical and ferroelectric properties of nano crystalline ZnO.

1.3) HISTORICAL PRESPECTIVE

1.3.1) THE HISTORY OF PHOSPHORS

The history of phosphors can be divided into four generations. [14]

a) First Generation Phosphor:

The earliest fluorescent tubes employed a phosphor of Zinc Beryllium Silicate – the first material found to create white light with reasonable quality. However the efficiency was very less near about 35 lumens per watt. These phosphors were rapidly superseded once more efficient materials had been developed. These phosphors were used before 1948. The materials used in this generation were basic sulphide, tungstate and molybdate.

b) Second Generation Phosphor:

The most commonly found tubes on the global lighting market employ an internal coating of Calcium Halo phosphate materials (generally known simply as 'Halo phosphate' tubes). This revolutionary material was invented in 1942 by a group led by A.H. McKeag of Osram-GEC in London, and succeeded in almost doubling lamp efficiency.

However by modern standards, the Halo phosphate materials are relatively inefficient and deliver inferior lighting quality compared to newer technologies. Although such tubes have a low initial purchase cost, this is rapidly offset by the increased electrical power consumption required to generate a given amount of light. A wide variety of different whites can be created by the Halo phosphate system. The phosphor is in fact a blend of two different materials which radiate broadly in the blue and orange parts of the spectrum respectively. The color rendering index is typically 50 to 70 and the lamp efficiency approx. 60 – 75 lm/W.

c) Third Generation Phosphor:

During the 1970's a great deal was learned about human vision systems, and this spurred fluorescent research into new territories. Traditionally it had been believed that to achieve good color rendering, it was important for the lamp to produce a full spectrum with light

of all wavelengths present. However the human eye is not equally sensitive to all colors. Therefore if a lamp is built to radiate all wavelengths, much of it will occur in regions to which the eye is less sensitive. New insights into the perception of color vision discovered that it should be possible to achieve a very high color rendering index from a light source having a narrow tri-band spectrum. These three bands correspond to the ***RED, GREEN and BLUE photo-receptors*** in the eye.

It was theoretically proposed by the Westinghouse Company in the USA to develop a prime-color tube with three peaks at ***450nm (blue), 540nm (green) and 610nm (orange***) to coincide with the mechanisms of human color vision. As shown below in Fig.1.2

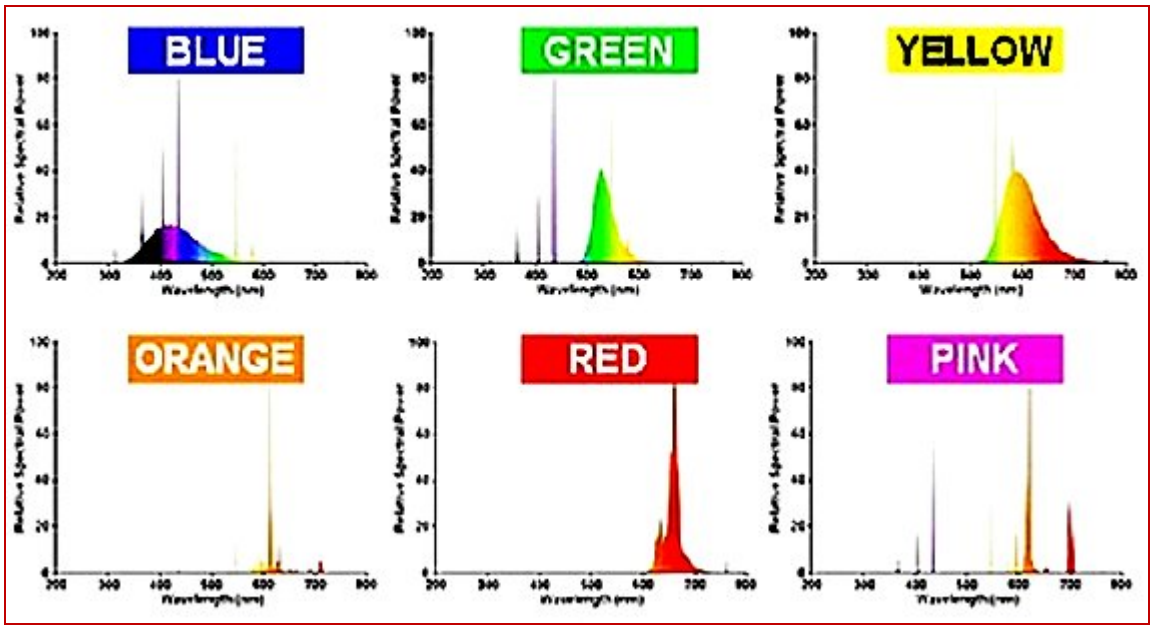

Fig.1.2 Spectra of some common tube colors

By blending together the blue, green and red components in the correct proportions, a net white output of various hues can be realized. An unexpected advantage of these deeply saturated colored phosphors was their astonishing efficiency of converting UV into visible light. As a result lamp efficacy is boosted to levels of around 80 – 95 lm/W. Perhaps the only reason for the lack of penetration of triphosphor materials is their high cost.

d) Fourth Generation Phosphors:

Current research into light and its effects on the human psyche are continuing to drive lamp technology into exciting new areas which include **nanophosphors.** The research on such materials is still going on and expected to increase the efficiency of the lamp to about 98 lm/W. The balance of phosphors has been engineered to strike what is currently believed to be the optimal balance between light for vision and light for personal well-being.

1.3.2) THE HISTORY OF FERROELECTRICS

The history of ferroelectrics can be divided into 3 era's

a) The Early Rochelle Salt Period:

The object of this period of study was first separated in 1655 by Elie Seignette, an apothecary in the town of La Rochelle, France***. Sodium potassium tartrate tetrahydrate (Rochelle salt)*** was used for over 200 years for its mild purgative medicinal properties. Late in the nineteenth its physical properties began to excite interest. In 1824 Brewster had observed the phenomenon of pyroelectricity in various crystals, among which was Rochelle salt, but perhaps the first systematic study were those of the brothers Pierre and Paul-Jacques Curie in 1880.[15,16] This classic work established unequivocally the existence of the piezoelectric effect and correctly identified Rochelle salt and a number of other crystals as being piezoelectric.

Perhaps an appropriate culmination for the Rochelle Salt period came with a series of four papers by H. Mueller. Mueller for the first time distinguished the three possible origins for proper ferroelectricity in Rochelle. [17-20]

b) Intermediate KDP era:

The horizon for workers in ferroelectrics was significantly broadened in 1935 by Busch and Scherer report of the occurrence of ferroelectricity in ***Potassium dihydrogen phosphate*** and the isostructural dihydrogen arsenate. [21, 22] It is perhaps interesting to note that, as in Rochelle salt, the finer points of the kinetics of the changes at T_c remained puzzling for a long period. In KDP, however, Raman and NMR spectra later revealed the fascinating interconnection between the proton ordering and the soft mode in the motion of the potassium and phosphate ions which is the dominant carrier of spontaneous polarization.

c) Perovskite Era:

A minor accessory mineral, formula ***$CaTiO_3$***, occurring in basic rocks was found. Perovskite has given its name to a large family of materials, synthetic and natural, crystallizing in similar structures as that of $CaTiO_3$. The crystal structure is ideally cubic, with a framework of corner-sharing octahedra, containing titanium (Ti) or other relatively small cations surrounded by six oxygen (O) anions. Within this framework are placed calcium (Ca) or other large cations, surrounded by twelve anions as shown in Fig.1.3.

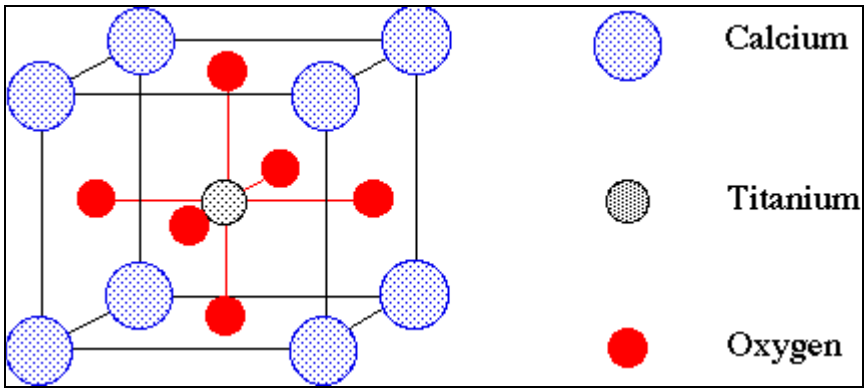

Fig.1.3 Crystal structure of $CaTiO_3$

Tilting of the octahedra and other distortions often lower the symmetry from cubic, giving the materials important ferroelectric properties and decreasing the coordination of the central cation. This flexibility gives the structure the ability to incorporate ions of different sizes and charges. Substitution of niobium (Nb), cerium (Ce), barium (Ba) and other rare-earth elements in natural calcium titanate ($CaTiO_3$) is common and can make Perovskite an ore for these elements.

By the early 1950's, ceramic piezoelectric transducers based on ***$BaTiO_3$*** were becoming well established in a number of both civil and military applications. $BaTiO_3$ has a curie temperature of 120^0c above which it becomes paraelectric. Following the wide success of the simple $BaTiO_3$-based ceramic transducer, that people starts examine other ferroelectric Perovskite compounds for potential applications. Some of the very early basic work was on pure ***$PbTiO_3$*** and ***$PbZrO_3$*** solid solution system. These posses very high value of Curie temperature 490 °C for $PbTiO_3$ and 233°C for $PbZrO_3$. The key studies, was of ***$PbTiO_3$:$PbZrO_3$*** solid solution system which established the PZT system as exceptionally suitable for the formulation of piezoelectrics. This work has been carried

out by Jaffe and coworker [23, 24] at the National Bureau of Standards. The number of applications expanded steadily during the next three decades and is now entering an age of integration and miniaturization in which three-dimensional ceramic circuitry is being developed. Further advances will undoubtedly occur in the years ahead as the field electroceramics of follows in the footsteps of the semiconductor industry which will lead to production of MEMS devices in which both electronics and the mechanical components are joined together. The electronics will serve as the brain of the device and the mechanical components will gives the actuators response. The practical applications of such devices involve:

a) Inkjet printers, which use piezoelectrics or thermal bubble ejection to deposit ink on paper.
b) Accelerometers in modern cars for a large number of purposes including airbag deployment in collisions.

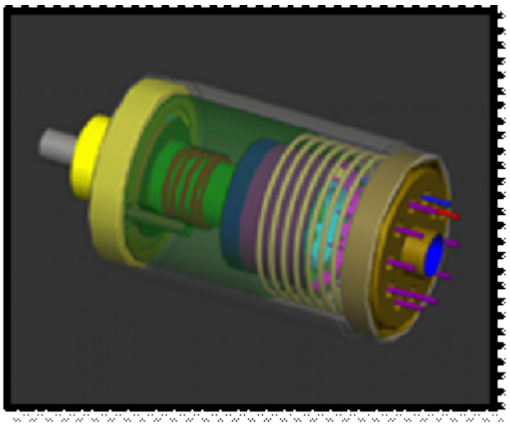

Fig.1.4a Accelerometer

Fig.1.4b Inkjet printer

CHAPTER 2

ORIGIN OF PHOSPHORESCENCE AND FERROELECTRICITY IN ZnO

2.1) PRINCIPLE OF PHOSPHORESCENCE:

Emission of light from a substance exposed to radiation and persisting as an afterglow after the exciting radiation has been removed is called phosphorescence. Unlike fluorescence, in which the absorbed light is emitted about 10^{-8} second after excitation, in phosphorescence the extra energy absorbed is stored in metastable states and re-emitted later. Phosphorescence is a specific type of photoluminescence related to fluorescence. Unlike fluorescence, a phosphorescent material does not immediately re-emit the radiation it absorbs. As these transitions occur less often in certain materials, absorbed radiation may be re-emitted at a lower intensity for up to several hours. [25]

Most photoluminescent events, in which a chemical substrate absorbs and then re-emits a photon of light, are fast, of the order of 10 nanoseconds. However, for light to be absorbed and emitted at these fast time scales, the energy of the photons involved (i.e. the wavelength of the light) must be carefully tuned according to the rules of quantum mechanics to match the available energy states and allowed transitions of the substrate***. In the special case of phosphorescence (for organic molecules),*** the absorbed photon energy undergoes an unusual intersystem crossing into an energy state of higher spin multiplicity. [26, 27] As shown in Fig.2.1

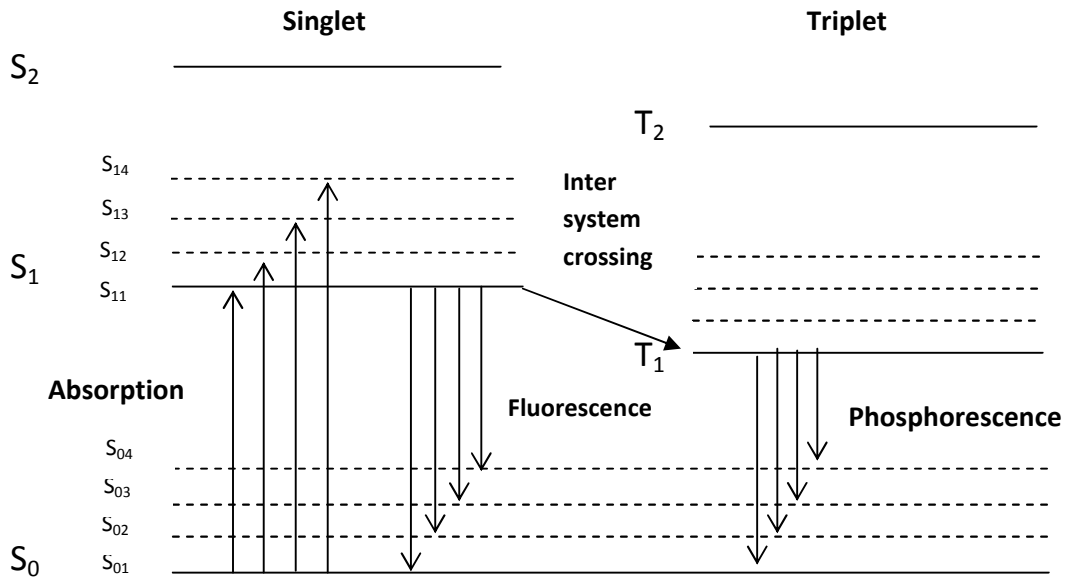

Fig.2.1 Jablonski Diagram

As a result, the energy can become trapped in the triplet state with only classically "forbidden" transitions available to return to the lower energy state. These transitions, although "forbidden", will still occur in quantum mechanics but are kinetically unfavored and thus progress at significantly slower time scales. The energy equation thus can be given as

$$S_0 + h\nu \rightarrow S_1 \rightarrow T_1 \rightarrow S_0 + h\nu'$$

Where 'S' Denote Singlet and 'T' denote Triplet States

Transitions can also occur to higher energy levels, but the first excited state is denoted for simplicity. Fig.2.2 shows the fused silica blue phosphor excited by UV.

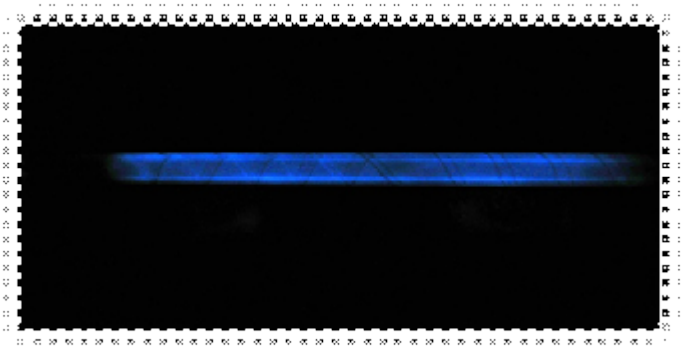

Fig.2.2 Fused silica blue phosphor excited by UV

On the other hand, the photoluminescence in ZnO (or metal oxides) is explained on the basis of the "band model". ZnO is a popular and useful semiconductor material. In addition, ZnO has a so-called "direct band-gap," unlike Si which has an indirect band-gap. This results in a strong interaction with light which makes it useful for generating light in LEDs (light emitting diodes) and laser diodes. [28]

In order to understand the concept of a *gap* in energy, first consider that some of the electrons in a solid are not firmly attached to the atoms, as they are for single atoms, but can hop from one atom to another. These loosely attached electrons are bound in the solid by differing amounts and thus have much different energy. Electrons having energies above a certain value are referred to as ***conduction*** electrons, while electrons having energies below a certain value are referred to as ***valence*** electrons. This is shown in the Fig.2.3 where they are labeled as conduction and valence *bands*. The word band is used because the electrons have a multiplicity of energies in either band (*means, electrons which are mobile in a solid posses kinetic energy which varies with their*

velocity (1/2 mv^2). Thus, because of their motion they have a multiplicity of energies and is referred to as a band of energies.). Furthermore, there is an energy *gap* between the conduction and valence electron states. Under normal conditions electrons are forbidden to have energies between the valence and conduction bands. [29]

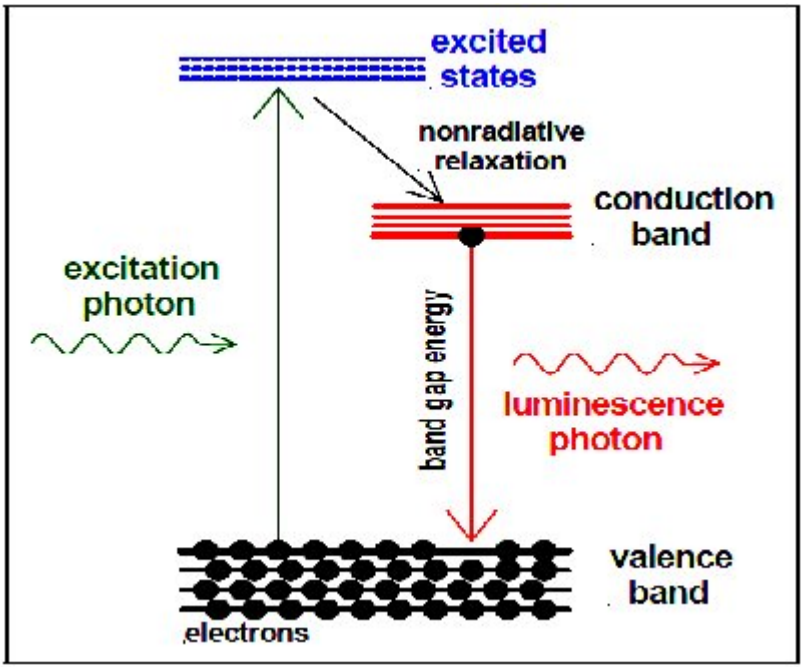

Fig.2.3 Band diagram for ZnO explaining Photoluminescence

If a light particle (photon) has energy greater than the band gap energy, then it can be absorbed and thereby raise an electron from the valence band up to the conduction band across the forbidden energy gap. In this process of photoexcitation, the electron generally has excess energy which it loses before coming to rest at the lowest energy in the conduction band by some non radiative transition. At this point the electron eventually falls back down to the valence band. As it falls down, the energy it loses is converted back into a luminescent photon which is emitted from the material. The process of photon excitation followed by photon emission is called ***photoluminescence*** and since it is delayed one then it is often called as the **phosphorescence.**

2.2) APPLICATIONS OF PHOSPHORS:

The applications of the phosphors include

1) Lighting:

Phosphor materials play a major role in the lighting. The layers of phosphor material in the fluorescent lamps provide most of the light to it and they are also used to improve the balance of light produced by metal halide lamp. Now days, they found application in the electroluminescent displays for example- in aircraft instrument panels. The electroluminescent display consists of a phosphor layer sandwiched between two insulators to limit the current and driven with alternating current at high fields. Fig. 2.4 shows mechanistically how this device works.

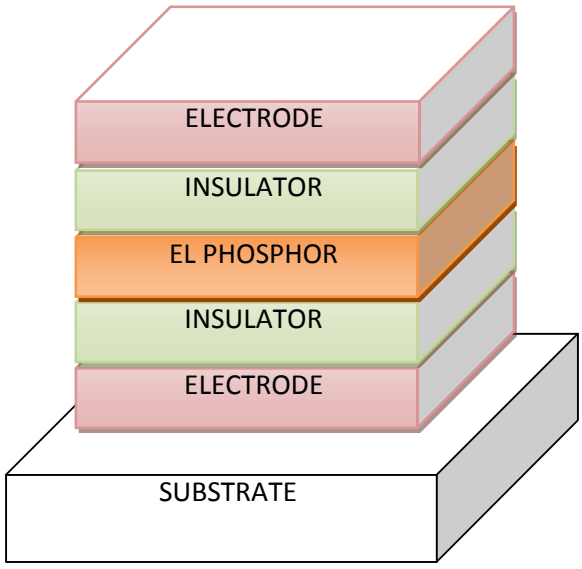

Fig.2.4 Electro-luminescent display device configuration

2) Cathode ray tube (CRT)

A cathode ray tube (CRT) is a specialized vacuum tube in which images are produced when an electron beam strikes a phosphorescent surface. Most desktop computer displays make use of CRTs. A cathode ray tube consists of several basic components, as illustrated in Fig.2.5. The electron gun generates a narrow beam of electrons. The anodes accelerate the electrons. Deflecting coils produce an extremely low frequency

electromagnetic field that allows for constant adjustment of the direction of the electron beam.

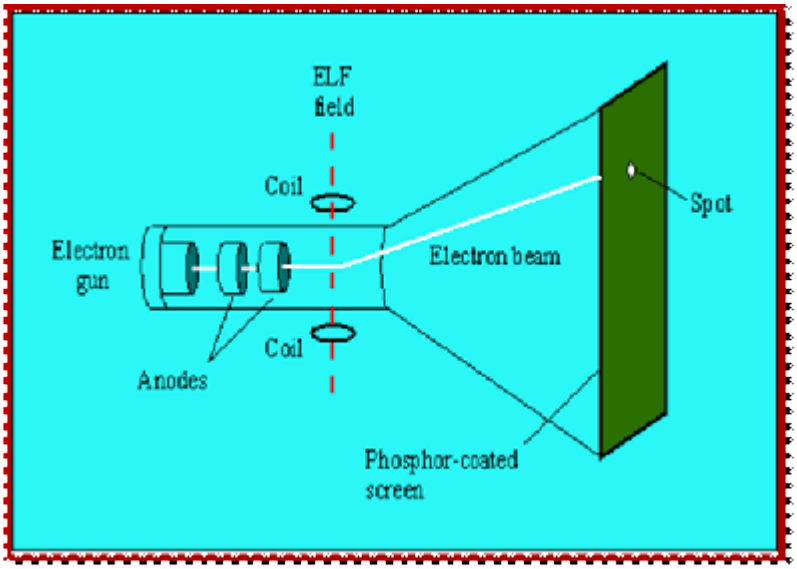

Fig.2.5 Cathode Ray Tube

The intensity of the beam can be varied. The electron beam produces a tiny, bright visible spot when it strikes the phosphor-coated screen. To produce an image on the screen, complex signals are applied to the deflecting coils, and also to the apparatus that controls the intensity of the electron beam. This causes the spot to race across the screen from right to left, and from top to bottom, in a sequence of horizontal lines called the raster. As viewed from the front of the CRT, the spot moves in a pattern similar to the way our eyes move when we read a single-column page of text. But the scanning takes place at such a rapid rate that your eye sees a constant image over the entire screen.

The illustration above shows only one electron gun. This is typical of a monochrome, or single-color, CRT. However, virtually all CRTs today render color images. These devices have three electron guns, one for the primary color **RED**, one for the primary color **GREEN**, and one for the primary color **BLUE**. The CRT thus produces three overlapping images: one in red (R), one in green (G), and one in blue (B). This is the so-called RGB color model.

3) Phosphor Thermometry:

Phosphor thermometry is a temperature measurement approach that utilizes the temperature dependence of certain phosphors for this purpose. For this, a phosphor coating is applied to a surface of interest and, usually, the decay time is the emission parameter that indicates temperature. Certain characteristics of the emitted light change with temperature, including brightness, color, and afterglow duration. Method of temperature detection is based on intensity ratios of two separate emission lines; the change in coating temperature is reflected by the change of the phosphorescence spectrum. Furthermore, Thermal barrier coating can yield a micro probe to detect the aging mechanisms or changes to other physical parameters that affect the local atomic surroundings of the optical active ion for example- detecting hot corrosion processes in Yttria-stabilized zirconia. [30-32]

4) Glow in the dark toys:

If the phosphorescent quantum yield is high, these substances will release significant amounts of light over long time scales, creating so-called "glow-in-the-dark" materials. As shown in Fig.2.6. Typical materials which produces such effect has been listed below in Table.2.1

Fig.2.6 Glow in the dark toys

Table 2.1 Materials producing Phosphorescence

S.No	Material	Color
1)	Calcium sulfide with strontium sulfide with bismuth as activator, (Ca,Sr)S:Bi	BLUE light with glow times up to 12 hours
2)	Strontium Aluminate activated by Europium	GREEN
3)	Strontium sulfide	RED
4)	$SrAl_2O_4$:Eu(II):Dy(III)	AQUA

2.3) PRINCIPLE OF FERROELECTRICITY IN ZnO:

ZnO is a tetrahedrally bonded semiconductor, posse's ferroelectric properties and shows a strong piezoelectric response. The ferroelectricity in ZnO can be explained on the basis of its non-centro symmetric crystal structure. ZnO has a wurtzite structure with lattice parameters a=b= 0.3296 nm and c= 0.5207 nm. It is made up of a number of alternating planes composed of tetrahedral Zn^{2+} and O^{2-} ions along c axis. [33] Due to this tetrahedral coordination, it shows non-centro symmetric crystal structure, which in turn gives rise to ferroelectricity in zinc oxide. The crystal structure and polarization direction has been shown below in Fig.2.7

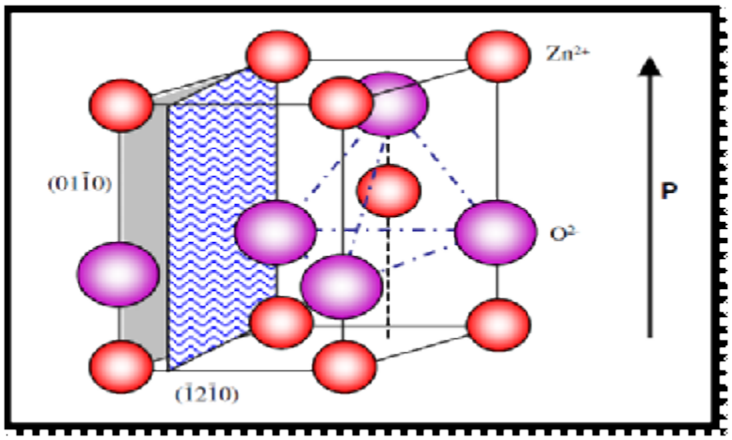

Fig.2.7 Crystal structure and polarization direction in ZnO

The oppositely charged ions produce positively charged (0001) Zn and negatively charged (0001) O polar surface respectively. These polar surfaces give rise to dipole moment and a spontaneous polarization along the c axis. To maintain a stable structure, usually the polar surfaces undergo massive surface reconstruction but zinc oxide polar surfaces are automatically stable without undergoing any reconstruction. [34, 35] Other two most commonly observed facets are (2 1 1 0) and (0 1 1 0) which are non polar and have lower energy than that of polar surfaces. Nanostructure of Zinc Oxide generally grows within these non polar surfaces. [36-38] ZnO is structurally simple and easy to fabricate therefore, ZnO has been widely used in microelectromechanical systems as sensors and actuators and in communication field as surface acoustic wave devices.

On doping of divalent cation Zinc sites by some high valency ions creates mixed valency as well as strain in the original ZnO hexagonal structure. The mixed valency creates charge polarity between Zn-O and M-O bonds. This charge polarity and the rotation of the non linear M-O bonds with respect to Zn-O bonds under electric field shows the ferroelectric properties, in most of the cases Vanadium doping has been already done and well studied. [39] Fig.2.8 shows how Zinc ion is substituted by Vanadium ion.

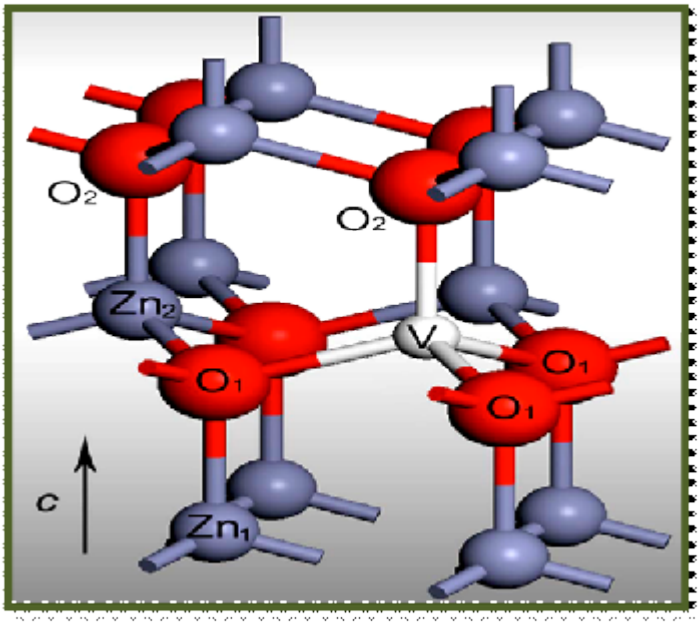

Fig.2.8 Vanadium substitution on Zinc site

2.4) APPLICATIONS OF FERROELECTRICS:

1) Capacitors:

A capacitor consists of a dielectric material sandwiched between two electrodes. The total capacitance for this device is given by

$$C = (\varepsilon_0 \varepsilon_r A) / d$$

Where, **C= Capacitance, ε_0 = Permittivity of free space, ε_r = Permittivity of the medium, A= Area of the electrode, d= distance between the electrodes**

To get a high volumetric efficiency (capacitance per unit volume) the dielectric material between the electrodes should have a large dielectric constant, a large area and a small thickness. The volumetric efficiency can be further enhanced by using multilayer ceramic (MLC) capacitors. As shown in Fig.2.9, the MLC capacitor structure consists of alternate layers of dielectric and electrode material. Each individual dielectric layer contributes capacitance to the MLC capacitor as the electrodes terminate in a parallel configuration and thus the individual capacitances will add up. Hence the effective equation for capacitance becomes,

$$C = n (\varepsilon_0 \varepsilon_r A) / d$$

Where, **n= Number of dielectric layers.**

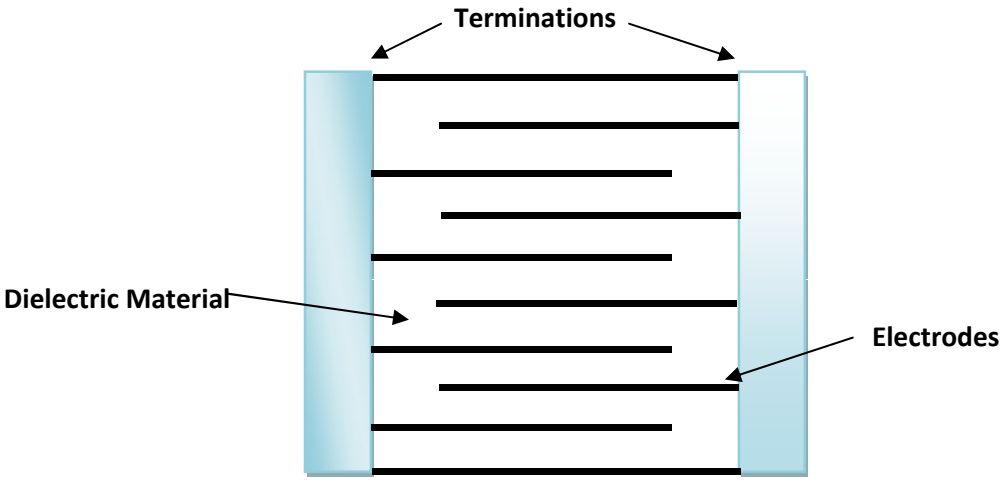

Fig.2.9 Multilayer capacitor.

2) **Non- volatile memory:**

Semiconductor memories such as dynamic random access memories (DRAM's) and static random access memories (SRAM's) currently dominate the market. However, the disadvantage of these memories is that they are volatile, i.e. the stored information is lost when the power fails. The non-volatile memories available at this time include complementary metal oxide semiconductors (CMOS) with battery backup and electrically erasable read only memories (EEPROM's). These non-volatile memories are very expensive. The main advantages offered by ferroelectric random access memories (FRAM's) include non-volatile and radiation hardened compatibility with CMOS and GaAs circuitry, high speed and high density. Ferroelectric materials spontaneously polarize on cooling below the T_c. The magnitude and direction of polarization can be reversed by the application of an external electric field. The FRAM's made from ferroelectric thin films make use of this phenomena to store data. The FRAM operates on the basis of polarization switching; the ferroelectric material should have a large remnant polarization and a small coercive field. The prospects of FRAM devices replacing the semiconductor memories in the near future are very bright and finally the storage device should be reliable.

3) **Piezoelectric for ultrasound imaging and actuators:**

Piezoelectric materials can be used for both active and passive transducer applications. In the passive mode the transducer acts as a sound receiver i.e. there is conversion of sound energy into an electrical signal. The converse piezoelectric effect permits a transducer to act as an active sound transmitter. In the pulse echo mode, the transducer is used to perform both the active and passive functions at the same time. A sound wave is propagated into the medium and a faint echo is received back after a small time gap due to the acoustic impedance mismatch between the interface materials. This principle is used in transducers for ultrasonic medical imaging applications.

The transducer is exited by an electrical signal which in turn produces a vibrational pulse in the medium to be interrogated (in this case the body). If the ultrasonic wave encounters impedance in the direction of propagation, part of the energy is reflected back towards

the transducer. This reflected echo produces a voltage signal which is used to generate the image of the internal organs and tissues in the body. The acoustic impedance difference between one tissue to another is small so the vibrational pulse penetrates to larger depths and gives a good imaging capability. Fig.2.10 shows a Piezoelectric transducer.

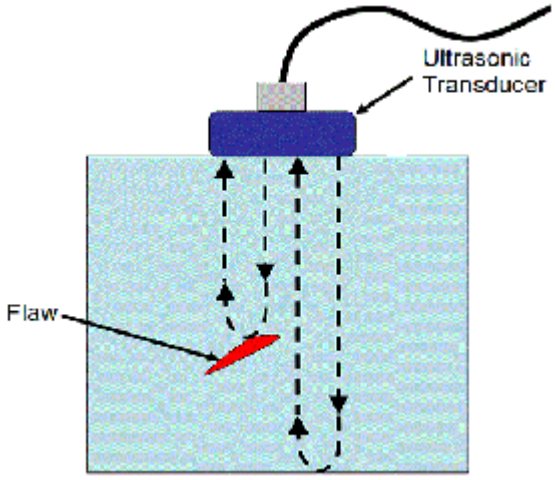

Fig.2.10 Piezoelectric transducer

4) Crystal Oscillators:

A **crystal oscillator** is an electronic circuit that uses the mechanical resonance of a vibrating crystal of piezoelectric material to create an electrical signal with a very precise frequency. This frequency is commonly used to keep track of time (as in quartz wristwatches), to provide a stable clock signal for digital integrated circuits, and to stabilize frequencies for radio transmitters and receivers. The most common type of piezoelectric resonator used is the ***quartz crystal,*** so oscillator circuits designed around them were called "crystal oscillators". Quartz crystals are manufactured for frequencies from a few tens of kilohertz to tens of megahertz. When a crystal of quartz is properly cut and mounted, it can be made to distort in an electric field by applying a voltage to an electrode near or on the crystal. When the field is removed, the quartz will generate an electric field as it returns to its previous shape, and this can generate a voltage. The result is that a quartz crystal behaves like a circuit composed of an inductor, capacitor and resistor, with a precise resonant frequency.

2.5) LITERATURE REVIEW:

The work on the ***Phosphors*** materials begins after the French physicist Alexandre E. Becquerel investigated the phenomena of fluorescence and phosphorescence in 1857. In 1901 Peter Cooper Hewitt from America patented (U.S. patent 889,692) the first mercury vapor lamp. The low pressure mercury arc lamp of Peter Cooper Hewitt is the very first prototype of today's modern fluorescent lights. In 1927 a real breakthrough was introduced by Edmund Garmer of Germany who patented an experimental fluorescent lamp. In the continuous progress in this field George Inman and Richard Thayer designed the first practical and viable fluorescent lamp (U.S. Patent No. 2,259,040) that was first sold in 1938. Thereafter, in 1942 A.H. McKeag of Osram-GEC in London succeeded doubling lamp efficiency and introduces *Calcium Halo phosphate*, a new revolutionary material for fluorescent lamps.

In 1970's a great focus was given about human vision systems, and this leads fluorescent research into new dimensions. In 1970 C. H. Henry and et al. [40] has studied the Li and Na substitution in CdS and CdSe. Results indicate that Li and Na are the shallow acceptors in CdS and CdSe. Keeping in view that the 'S' and 'Se' are harmful compounds in 1976 Red emission was reported to exhibit in ion implanted ZnO by B.J. Pierce and R.L. Hengehold. [41]

In 1992 Mi Liu and et al. [42] reported the green emission (around 520 nm) of the cathodoluminescence of ZnO, which was attributed to Zn interstitials. The origin of the green emission is still a subject of controversy. Various models have been proposed such as Zn interstitials (Zn_i), O vacancies (V_0), interstitial O (O_i) etc.

In the year 1995 Yasufumi Hayashi and et al. [43] has studied the photoluminescence in Eu^{3+} doped ZnO phosphor and obtain red band luminescence. They also reported that the intensity and fine structures of Eu^{3+} luminescence are strongly influenced by the doping conditions.

Up to 1998 there are many reports concerning the luminescent properties of ZnO but most of the work has been done on bulk samples and powder phosphor usually pressed in pellets and sintered at high temperatures (800-1400^{0}C). [44,45] In 1998 S.A. Studenikin and et al. [46] prepared undoped ZnO thin films using spray pyrolysis method and reported green and orange photoluminescent properties. They reported that green photoluminescent films possessed a

porous structure while orange films possessed a close packed granular morphology. The result reveals that green luminescence appear due to the oxygen vacancies. In 2001 A. A. Bol and et al. [47] suggest that nanocrystals of II-VI semiconductors are unique host materials for the doping of optically active impurities, and semiconductor nanocrystals doped with luminescent centers exhibit efficient luminescence even at room temperature. In 2005 Atsushi Ishizumi and et al. [48] fabricate ZnO: Eu nanorods by micro emulsion technique reported a sharp luminescence due to the intra-4f transitions of Eu^{3+}.

In 2008 Yinzhen and et al. [49] successfully grows ZnO thin films on CaF_2 substrate by magnetron sputtering and reported that these films exhibit strong U.V near-band-edge emission peak at 376.5 nm and weak visible red emission at 643.49 nm. In 2008 P.Kumbhakar and et al. [50] prepared monodispersed PVP capped nanoparticles of ZnO in double distilled water. A strong green photoluminescence emission under U.V excitation of 320 nm is reported from the prepared ZnO nanoparticles due to the recombination of a photo-generated hole with a single ionized charge state. In the same year Li Chen and et al. [51] studied Optical properties of trivalent europium doped ZnO prepared by solid state reaction route under indirect excitation of near UV light. The results suggest that there exists prominent energy transfer from ZnO host to Eu^{3+} ions. A series of energy levels as temporary storage of excitation energy play a crucial role on this energy transfer process.

Recently, in 2009 Zhang Fu- Chun and et al. [52] studied the principle of optical properties in ZnO nanowires and they reported that band gap, binding energy show great dimension and size effects. They also found that dielectric functions of ZnO nanowires have different peaks with respect to light polarization and the peaks of ZnO nanowires exhibit a significant blue shift in comparison with those of bulk ZnO. In the same year Y. Dongqi and et al. [53] investigated the Photoluminescence of Phosphor doped ZnO nanotetrapods synthesized by chemical vapor deposition technique in which P_2O_5 is chosen as dopant source. The PL spectrum of the phosphorus-doped sample at 10K exhibited several acceptor-bound exciton related emission peaks. The acceptor-binding energies of the phosphorus dopant were estimated to be about 120 MeV, in good agreement with the corresponding theoretical and experimental values. They concluded that the development of phosphorus-doped ZnO nanotetrapods through a process

involving low-cost P_2O_5 as the dopant source will enable the fabrication of p-type ZnO-based nanodevices.

On the basis of above literature review for the phosphor materials we can say that inspite of lot of work has been carried out on the ZnO as a phosphor material, still the nanostructures of ZnO are under examination. It is clear from the literature review that the luminescent properties of ZnO largely depend on doping, morphology and crystallite size, so a lot of stress has to been given on the choice of dopant, control of morphology and crystallite size which can be easily tuned by controlling the conditions of the reaction.

On the other hand, it was Brewster who claims the phenomenon of pyroelectricity in various crystals in 1824, among which Rochelle salt was the first material to exhibit **ferroelectricity.** Later on with the continuous growth in the field perovskite materials like $BaTiO_3$, $CaTiO_3$, $PbTiO_3$, PZT etc. has also been found which exhibit strong ferroelectric properties. These systems have been extensively studied while the ferroelectricity in nonperovskite semiconductor material like ZnO still do exists and facilitates many technological applications.

In 1998 A. Onodera and et al. [54] has studied the Ferroelectricity in Li-substituted ZnO and reported a ferroelectric phase transition temperature T_c is 470 K in hot-pressed ceramics synthesized by the spark plasma sintering method, although the previous cold-pressed ceramics showed a relative low T_c (330 K). The ferroelectricity in Li substituted ZnO results from small structural distortion (of order 10^{-3} A) induced along the polar c-axis by substitutional Li atoms.

In 1999 M Joseph and et al. [55] reported the ferroelectric behavior in Li- doped ZnO thin films prepared by pulsed laser deposition grown on Si substrate. The peak maximum in the capacitance- temperature curve suggests the presence of ferroelectricity and the observed T_c is at 340 K. Moreover, hysteresis character is observed in C-V measurements.

In 2002 A. Onodera report ferroelectricity in Li, Mg, Be substituted ZnO and report that T_c increases with the increase in the Li doping. The dielectric results shows that the introduction of Mg^{2+} suppress the T_c while Be^{2+} shows the same value of the T_c.

In 2004 M H Zhao and et al. [56] suggested d_{33} coefficient as an important parameter evaluating piezoelectric performance and reported d_{33} coefficient of pure ZnO is 9.9 pmV^{-1} for the bulk ,

12.4 pmV^{-1} for an oriented film and 26.7 pmV^{-1} for nanobelts which is approximately one order of magnitude lower compared with prevalent piezoelectric perovskite ceramics.

In 2006 M. Alexe and et al. [57] studied ferroelectric behavior in nanotubes and metal-ferroelectric-metal composite nanotubes using silicon and ZnO nanowires as positive templates. The results show piezoelectric hysteresis loops and ferroelectric switching. They suggested that fabrication approach can be used to fabricate three-dimensional capacitors for ferroelectric nonvolatile memories as well as nanosize piezoelectric scanners and actuators. In the same year Dhananjay and et al. [58] studied the effect of Li substitution on dielectric and ferroelectric properties of ZnO thin films grown by pulsed-laser ablation. The results reveal that highly *c*-axis-oriented films were obtained at a growth temperature of 500 °C. The spontaneous polarization (*Ps*) and coercive field (E_c) of 0.6 $\mu C/cm^2$ and 45 kV/cm were obtained for $Zn_{0.85}$ $Li_{0.15}$ O thin films.

In 2008 Y C Yang and et al. [59] reported an enhanced d_{33} coefficient value of 110 pm V^{-1} for ZnO thin films doped with vanadium prepared on Si(111) substrates by direct current reactive magnetron co sputtering, which becomes comparable with the piezoelectric Perovskite ceramics, indicating that the performances of available doped ZnO devices would get a qualitative improvement and could add a dimension to its application field.

Recently, in 2010 YQ Chen and et al [60] studied vanadium-doped ZnO piezoelectric nanofiber prepared by electrospinning method and reported a large value of d_{33} coefficient of 121 pm V^{-1} for nanofibers of ZnO. These nanofibers have diameter from 50 to 300 nm along the nanofiber length. A butterfly-shaped piezoelectric response was measured by scanning force microscopy. The large value of the piezoelectric coefficient may be attributed because of switchable spontaneous polarization induced by V dopants and the easier rotation of V–O bonds under an electric field.

In 2010 C.W. Zou and et al. [61] studied room temperature ferromagnetism and ferroelectricity behavior in (Cu, Li) co-doped ZnO films deposited by reactive magnetron sputtering technique. The result indicate that The sputtered $Zn_{0.90}Cu_{0.05}Li_{0.05}O$ film shows multiferroic properties exhibiting a saturated ferroelectric loop with a remanent polarization of 6 $\mu C/cm^2$ and a saturated loop with a saturation magnetization of 0.43 μ_B/Cu at room temperature. On the basis of above

literature review for the ferroelectrics we can conclude that ZnO is a promising material for ferroelectric devices. The ferroelectric property in ZnO can be tuned easily by doping with different elements and can be made comparable with that of the perovskite materials. Moreover, ZnO nanostructure can be used to fabricate three-dimensional capacitors for ferroelectric nonvolatile memories as well as nanosize piezoelectric scanners and actuators and are promising candidate for the realization of nanoscale piezoelectric devices in the MEMS applications.

2.6) GAPS IN THE STUDY:

From the literature review, it is clear that luminescence characteristics of the phosphor material are highly dependent upon doping, morphology and crystallite size. These are the aspects need more experimentation to improve the luminescence characteristics of phosphor material. Moreover, for improving the ferroelectric properties the dopant should induce a large amount of polarization and switching property. The charge and size of the dopant play a major role to induce polarization in the material. Keeping all these facts in mind an attempt shall be made to tailor such a material having diverse morphology, small crystallite size and possess ferroelectric characteristics.

2.7) OBJECTIVE:

- Synthesis of pure and modified ZnO.
- Structural, morphological, chemical and luminescence characterization of modified ZnO.
- Investigation of dielectric and ferroelectric properties in modified ZnO.

2.8) SIGNIFICANCE AND RELEVANCE OF THE STUDY:

Photoluminescent and ferroelectric devices are in demand for a rapidly growing range of applications. II-VI semiconductors have recently attracted the most intensive research for many properties and potential applications in building optical and optoelectronic nanodevices. The main advantage of these materials are their low price, high sensitivity and low power consumption. The most common applications of phosphor material are cathode ray tube, Field Emission Display, electroluminescent devices and glow in the dark toys. The presence of ferroelectricity in such materials has lead to evolution of piezoelectric transducers, multilayer capacitors, memory windows, SAW (sound acoustic wave) sensors

and fabrication of MEMS based devices. The nanostructured particles due to their high sensitivity and small crystallite size may provide suitable material for production of highly sensitive and fast response devices.

CHAPTER 3

RESEARCH METHODOLOGY AND CHARACTERIZATION TECHNIQUES

3.1) METHODOLOGY:

Chemical route is a versatile and economical route for growing thin films. We can also synthesize nano-structures materials by this route. This route is important because of facts like, high purity, low temperature synthesis, Good homogeneity and a narrow size distribution of the particles. The chemical synthesis consists of many known methods which include Chemical vapor deposition (CVD), Sol-Gel, Co-Precipitation, SILAR, Spray Drying, Spray pyrolysis, Freeze drying etc. In the present work co-precipitation technique has been used to synthesize pure and modified ZnO nanostructures.

3.1.1) PREAMBLE:

This method is a wet chemical method for the synthesis of colloidal dispersions of inorganic and organic-inorganic hybrid materials, particularly oxides. From these colloidal dispersions Powders, Fibers, Thin films and Monoliths can be prepared. Fabrication of different forms of final product required specific considerations but fundamental approach is the synthesis of colloidal dispersions is same.

This method comprises of 2 stages:

a) Hydrolysis:

The first stage of the sol gel method is called as the hydrolysis. In the hydrolysis reaction the metal alkoxides are hydrolyzed. The metal alkoxides has the general formula $M(OR)_Z$. Where, 'M' is metal and 'R' is alkyl group.

These alkoxides are prepared by the alcohol in which the hydroxide hydrogen is replaced by metal and therefore it is a metal-oxygen-carbon bond system.

$$M + z\,ROH \longrightarrow M(OR)_Z + z/2\,H_2 \quad \text{.....(1)}$$

The nature of alcohol has a significant effect on the reaction for e.g.: Sodium reacts vigorously with methanol and ethanol but the reaction is quite slow with isopropyl an extremely slow in tertiary butanol.

Now during the co-precipitation process the metal alkoxides first gets hydrolyzed. A water molecule interacts with the alkoxides and a molecule of alcohol is expelled out

$$M(OR)_Z + H_2O \longrightarrow M(OH)(OR)_{Z-1} + ROH \text{ .....(2)}$$

Metal alkoxides are soluble in their corresponding alcohols. In practice, dissolution of solid alkoxides is normally performed in corresponding alcohol.

$$M(OR)_Z + z\,R'OH \longrightarrow M(OR')_Z + z\,ROH \text{ .....(3)}$$

The reaction of this type is called as the alcoholic interchange or alcoholysis

It should be noted down that in the presence of the excess water, metal alkoxides form insoluble hydroxide or hydrated metal alkoxides depends upon metal for e.g.

$$Al(OR)_3 + H_2O \longrightarrow AlO(OH)\downarrow + 3\,ROH \text{.....(4)}$$

$$AlO(OH) + H_2O \longrightarrow Al(OH)_3\downarrow \text{ .....(5)}$$

The formation of insoluble precipitates as represented above makes it impossible polymerization to occur and shall be avoided.

b) Condensation:

In the condensation reaction the hydroxyl metal alkoxides product may react further to form polymerizable species.

Condensation results in the formation of nanoscale clusters of metal oxides or hydroxides often with groups embedded or attached to them.

$$M(OR)_{Z-1}(OH) + M(OR)_{Z-1}(OH) \longrightarrow (OR)_{Z-1}MOM(OR)_{Z-1} + H_2O \text{ …..(6)}$$

$$M(OR)_{Z-1}(OH) + M(OR)_Z \longrightarrow (OR)_{Z-1}MOM(OR)_{Z-1} + ROH\text{…..(7)}$$

The factors which have the severe effect on the reaction and the production of the suspension are listed below:

- pH
- Temperature and time of reaction

- Reagent concentration
- Nature and concentration of catalyst
- [H_2O/M] molar ratio
- Washing
- Aging temperature and time
- Drying

Moreover the reactivity of the metal atom is dependent largely on the extent of charge transfer and the ability to increase its co ordination number. As the electro negativity decreases the ability to increase its coordination number increases with their radii. The chemical reactivity of the corresponding alkoxides increases with their ionic radii.

There are several ways to ensure hetro condensation and achieve a homogeneous mixture of multiple components. Multiple step sol gel processing is yet another way to overcome this problem. In this the less reactive precursor is first hydrolyzed and more reactive precursor is hydrolyzed later. In order to deposit the thin films of the metal oxide different technique can be used, which include Dip Coating and Spin Coating techniques. As shown in the Fig.3.1

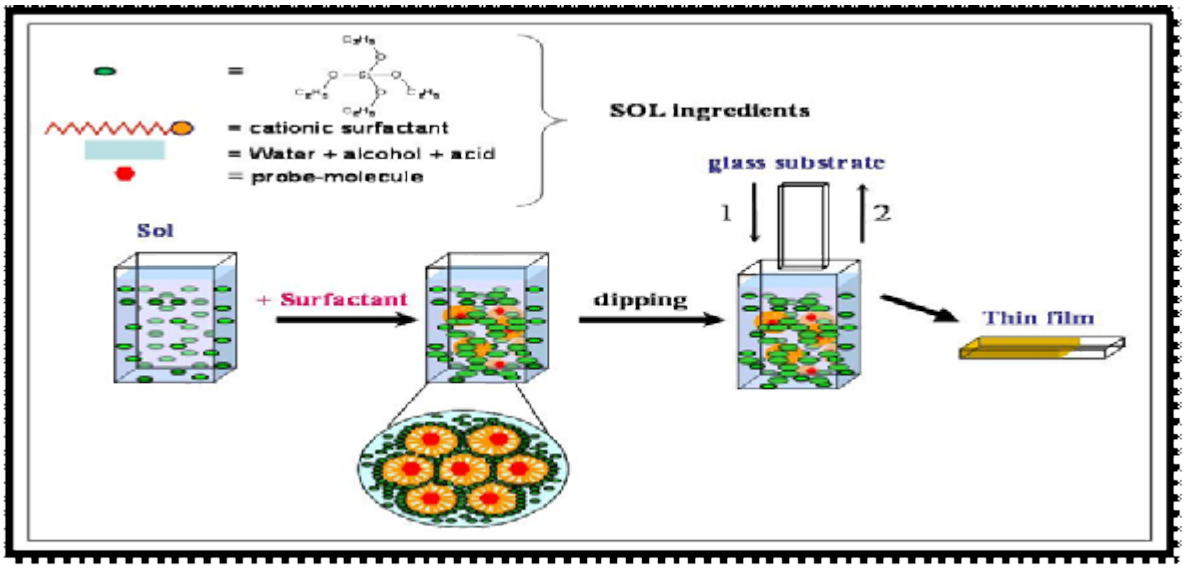

Fig.3.1 Deposition of film by dip coating

3.1.1) EXPERIMENTAL PROCEDURE:

a) Synthesis of Pure ZnO:

In order to achieve first objective samples of pure Zinc Oxide has been prepared by base catalyzed reaction using co-precipitation method. Zinc Acetate (Loba Chemie, purity 98.0%), Ethanol (Merck, purity 99.9%) and Sodium Hydroxide (Loba Chemie, purity 98.0%) were the materials used as a precursor, solvent and base for the synthesis of ZnO. All the materials were used as received without any purification.

Table 3.1 Requirement for synthesis of Pure ZnO

Chemical Name	Chemical Formula	Moles required(M)	Material Taken
Zinc Acetate	$Zn(CH_3COO)_2.2H_2O$	0.01	2.1970(g)
Ethanol	CH_3CH_2OH	.....	100 (ml)
Sodium Hydroxide	NaOH	0.02	0.8000(g)

Flow chart of Methodology:

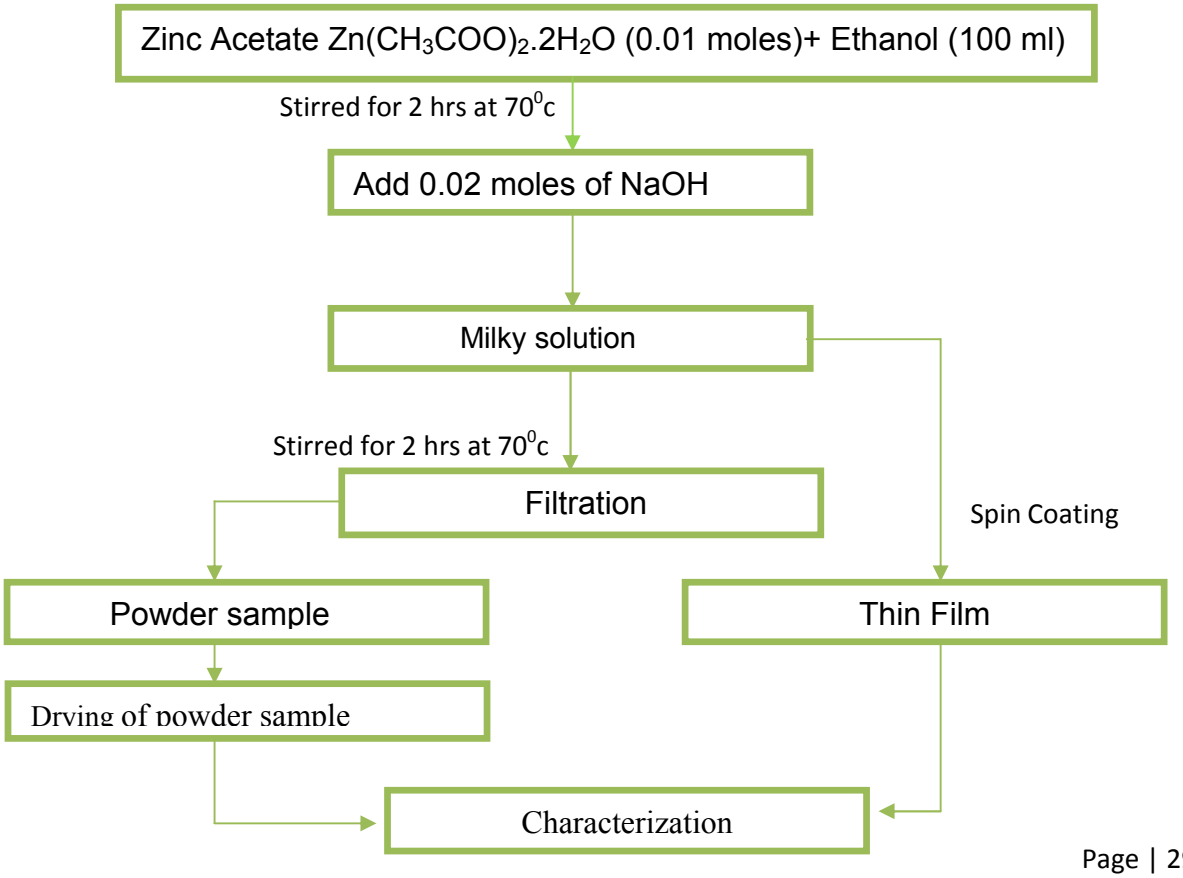

Detailed procedure

The steps involved for the synthesis of Pure ZnO are:

- In the 1st step 0.01 moles of Zinc Acetate [$Zn(CH_3CO_2)_2.2H_2O$] were dissolved in 100 ml of ethanol.
- The reaction temperature was maintained about 70^0c along with continuous stirring for 2 hours
- About 0.02 moles of NaOH added in the solution to adjust pH in basic region (10.82). The solution turns milky as shown in Fig.3.2 and the reaction mixture was allowed to stir for 2 hrs.

Fig.3.2 Experimental set up

- The precipitate thus obtained were filtered out and washed with ethanol many times.
- Finally, the obtained product was heated in the oven at 90^0c for 4 hours to remove the excess solvent and other residue material.
- The dried product was collected and grinded to make fine powder and finally characterized with many techniques.

b) Synthesis of Group III and Rare earth elements Doped ZnO:

Co-precipitation technique was employed to synthesize Group(III) and Rare earth element doped ZnO. In this reaction Zinc Acetate (Loba Chemie, purity 98.0%), Ethanol (Merck, purity 99.9%), Sodium Hydroxide (Loba Chemie, purity 98.0%) and dopants were taken in oxide form. We observe that doping of such elements is possible up to 3% as system does not hydrolyze excess amount of material used. The materials taken are shown in Table.3.2 and Table 3.3

Table 3.2 Chemical used for doping of Rare earth elements

CHEMICAL NAME AND REQUIREMENT									
	Zinc acetate dihydrated			**Sodium Hydroxide**	**Ethanol**	**Samarium Oxide**		**Europium Oxide**	
% age	Moles	Amount in grams	Molarity of solution (M)	Moles	Volume (ml)	Molarity of solution (μM)	Amount in grams	Molarity of solution (μM)	Amount in grams
Pure	0.01	2.197	0.1	0.02	100	…….	……	……	……..
0.25%	0.01	2.197	0.05	0.04	200	62.5	0.00435	62.5	0.0044
0.50	0.01	2.197	0.05	0.04	200	125	0.00871	125	0.0088
1%	0.01	2.197	0.05	0.04	200	250	0.01743	250	0.0176
3%	0.01	2.197	0.05	0.04	200	750	0.05231	750	0.0528

Table 3.3 Chemical used for doping of Group (III) elements

CHEMICAL NAME AND REQUIREMENT									
	Zinc acetate dihydrated			**Sodium Hydroxide**	**Ethanol**	**Titanium Dioxide**		**Niobium Pentaoxide**	
% age	Moles	Amount in grams	Molarity of solution (M)	Moles	Volume (ml)	Molarity of solution (μM)	Amount in grams	Molarity of solution (μM)	Amount in grams
Pure	0.01	2.197	0.1	0.02	100	……..	……	……..	……..
0.25%	0.01	2.197	0.05	0.04	200	125	0.00199	62.5	0.003322
0.50	0.01	2.197	0.05	0.04	200	250	0.00399	125	0.006645
1%	0.01	2.197	0.05	0.04	200	500	0.007989	250	0.01333
3%	0.01	2.197	0.05	0.04	200	1500	0.023967	750	0.03987

Flow chart of Methodology:

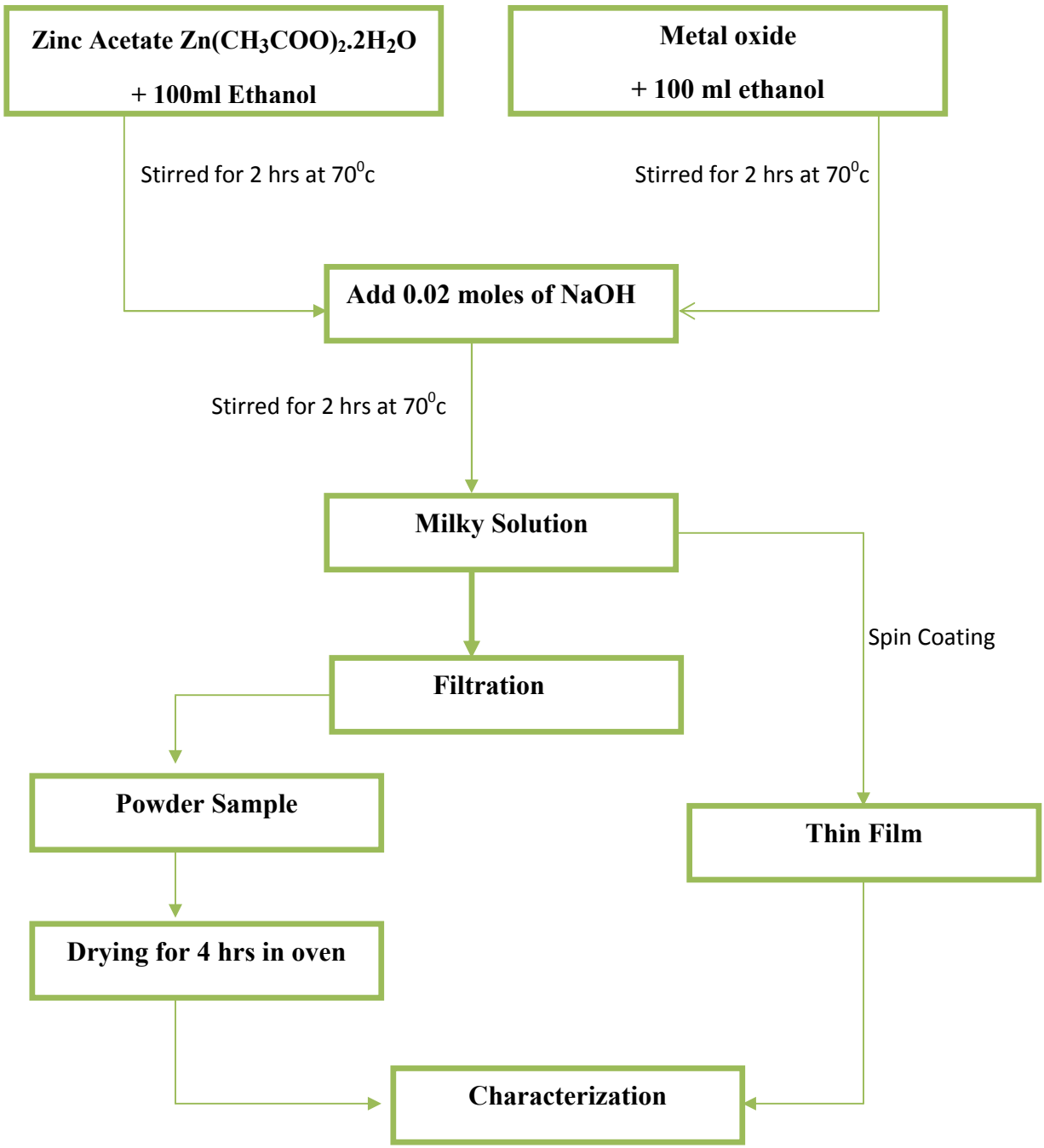

Detailed procedure:

The steps involved for the synthesis of Pure ZnO are

- In the 1st step 0.01 moles of Zinc Acetate [Zn $(CH_3CO_2)_2.2H_2O$] were dissolved in 100 ml of ethanol.
- In the 2nd step required no of moles of Metal oxide according to their composition were dissolved in 100 ml of ethanol
- About 0.02 moles of NaOH added in the solution to adjust pH in basic region (10.82). The solution turns milky as shown in Fig (3.2) and the reaction mixture was allowed to stir for 2 hrs.
- The precipitate thus obtained were filtered out and washed with ethanol many times.
- Finally, the obtained product was heated in the oven at 90^0c for 4 hours to remove the excess solvent and other residue material.
- The dried product was collected and grinded to make fine powder and finally characterized with many techniques.

3.2) CHARACTERIZATION TECHNIQUES

3.2.1) X-RAY DIFFRACTION METHOD

X-ray crystallography is a method of determining the arrangement of atoms within a crystal, in which a beam of X-rays strikes a crystal and diffracts into many specific directions. From the angles and intensities of these diffracted beams, a crystallographer can produce a three-dimensional picture of the density of electrons within the crystal. From this electron density, the mean positions of the atoms in the crystal can be determined, as well as their chemical bonds, their disorder and various other information.

In an X-ray diffraction measurement, a crystal is mounted on a goniometer and gradually rotated while being bombarded with X-rays, producing a diffraction pattern of regularly spaced spots known as *reflections* as shown in Fig.3.4. Crystals are regular arrays of atoms, and X-rays can be considered waves of electromagnetic radiation. Atoms scatter X-

ray waves, primarily through the atoms electrons. Just as an ocean wave striking a lighthouse produces secondary circular waves emanating from the lighthouse, so an X-ray striking an electron produces secondary spherical waves emanating from the electron. This phenomenon is known as elastic scattering, and the electron (or lighthouse) is known as the *scatterer* as shown in Fig.3.3. A regular array of scatterers produces a regular array of spherical waves. Although these waves cancel one another out in most directions through destructive interference, they add constructively in a few specific directions, determined by Bragg's law:

$$n\,\lambda = 2d\,\sin(\theta)$$

Where d= interplanner spacing

λ= Wave length.

θ= Brag's angle.

n= Order of reflections.

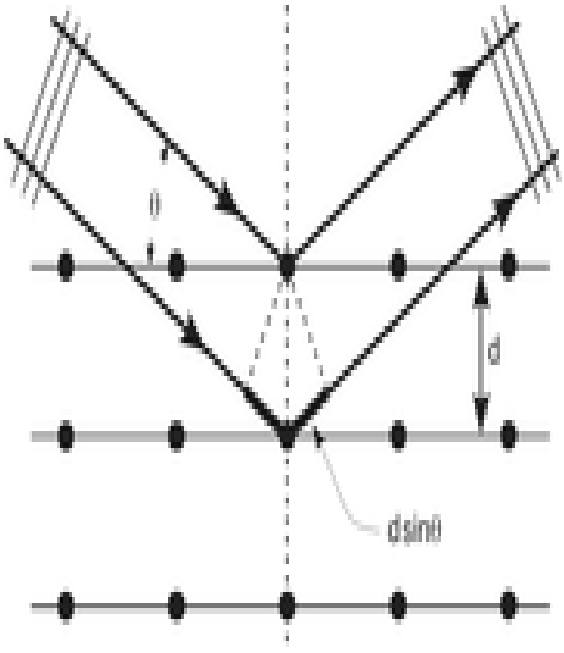

Fig.3.3 X- ray diffraction

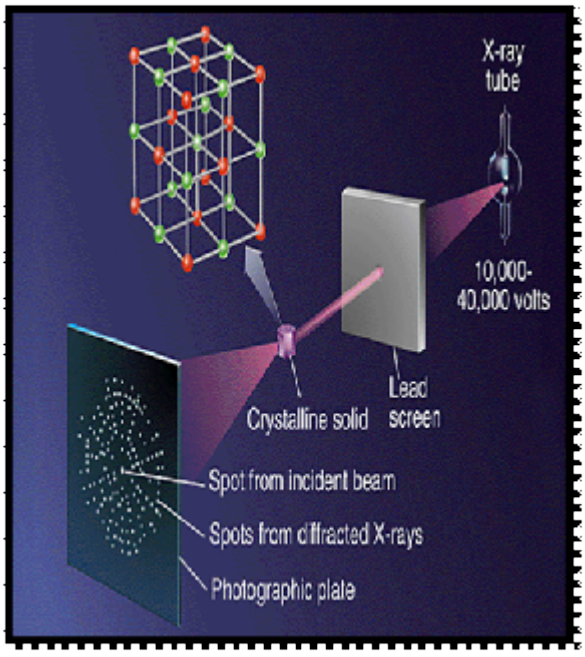

Fig.3.4 X- ray diffraction pattern

For the first order diffraction, n=1, and knowing the values of λ and θ, one can calculate the interplanar spacing d-value for a particular plane. After recording the X-ray diffraction pattern, first step involves the indexing of XRD peaks. The indexing means assigning the correct miller indexing to each peak of the diffraction pattern. The correct indexing is done only when all the peaks in the diffraction pattern are accounted for the process. There are three main methods for indexing a diffraction pattern

a) Comparing the measured XRD pattern with standard (JCPDS-cards)
b) Analytical methods
c) Graphical methods

In the case of fine particles, with the reduction in the size of the particles, the XRD lines get broadened, which indicates clearly that particle size has reduced. The line broadening can be a measure of the average size of the crystallites by using the scherer equation

$$\mathbf{D_v = (K\lambda) / b \cos(\theta)}$$

Where D_v is the average particle size,

K is the scherer costant,

λ is the wavelength

b is the integral breadth of the peak located located at the angle θ

Strengths and Limitations of X-ray Powder Diffraction (XRD)

Strengths

- Powerful and rapid technique for identification of an unknown minerals
- In most cases, it provides an unambiguous mineral determination
- Minimal sample preparation is required
- XRD units are widely available
- Data interpretation is relatively straight forward

Limitations

- Homogeneous and single phase material is best for identification of an unknown.
- Requires tenths of a gram of material which must be ground into a powder
- For mixed materials, detection limit is ~ 2% of sample
- For unit cell determinations, indexing of patterns for non-isometric crystal systems is complicated
- Peak overlay may occur and worsens for high angle 'reflections'

3.2.3) FOURIER TRANSFORM INFRARED SPECTROSCOPY

FT-IR stands for Fourier Transform Infrared, the preferred method of infrared spectroscopy. The prepared samples were characterized by FTIR spectroscopy. Fig.3.5 and Fig.3.6 shows the experimental set up. An infrared spectrum represents a fingerprint of a sample with absorption peaks which correspond to the frequencies of vibrations between the bonds of the atoms making up the material. Because each different material is a unique combination of atoms, no two compounds produce the exact same infrared spectrum.

Fig.3.5 FTIR Outside view

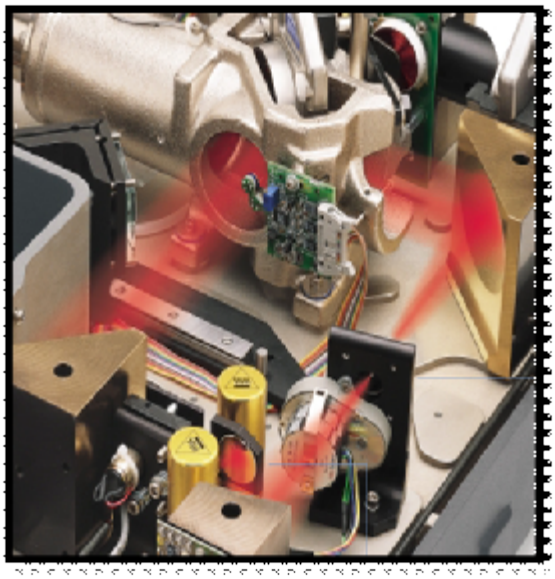

Fig.3.6 FTIR Inside view

In infrared spectroscopy, IR radiation is passed through a sample. Some of the infrared radiation is absorbed by the sample and some of it is passed through (transmitted). The resulting spectrum represents the molecular absorption and transmission, gives information of type of bonding in the sample.

• FTIR can identify unknown materials

• FTIR can determine the quality or consistency of a sample

• FTIR can determine the amount of components in a mixture.

The original infrared instruments were of the dispersive type. These instruments separated the individual frequencies of energy emitted from the infrared source. This was accomplished by the use of a prism or grating. A grating is a more modern dispersive element which better separates the frequencies of infrared energy. The detector measures the amount of energy at each frequency which has passed through the sample.

Fourier Transform Infrared (FT-IR) spectrometry was developed in order to overcome the limitations encountered with dispersive instruments. The main difficulty was the slow scanning process. A method for measuring all of the infrared frequencies simultaneously, rather than individually, was needed. A solution was developed which employed a very simple optical device called an interferometer. The interferometer produces a unique type of signal which has all of the infrared frequencies "encoded" into it. The signal can be measured very quickly, usually on the order of one second. Thus the time element per sample is reduced to a matter of a few seconds rather than several minutes.

3.2.3) U.V- VISIBLE SPECTROSCOPY

Ultraviolet-visible spectroscopy or ultraviolet-visible spectrophotometry (UV-Vis or UV/Vis) involves the spectroscopy of photons in the UV-visible region. This means it uses light in the visible and adjacent (near ultraviolet (UV) and near infrared (NIR)) ranges. The absorption in the visible ranges directly affects the color of the chemicals involved. In this region of the electromagnetic spectrum, molecules undergo electronic transitions. This technique is complementary to fluorescence spectroscopy, in that fluorescence deals with transitions from the excited state to the ground state, while absorption measures transitions from the ground state to the excited state.

This spectroscopy works on the principle of Beer-Lambert law .The Beer-Lambert law states that the absorbance of a solution is directly proportional to the concentration of the absorbing species in the solution and the path length. Thus, for a fixed path length, UV/VIS spectroscopy can be used to determine the concentration of the absorber in a solution. It is necessary to know how quickly the absorbance changes with concentration. The method is most often used in a quantitative way to determine concentrations of an absorbing species in solution, using the Beer-Lambert law:

$$A = -\log_{10}(I/I_0) = \epsilon \cdot c \cdot L$$

where A is the measured absorbance, I_0 is the intensity of the incident light at a given wavelength , I is the transmitted intensity, L the path length through the sample, and c the concentration of the absorbing species. For each species and wavelength, ε is a constant known as the molar absorptivity or extinction coefficient.

The basic parts of a spectrophotometer are a light source, a holder for the sample, a diffraction grating or monochromator to separate the different wavelengths of light, and a detector. The radiation source is often a Tungsten filament (300-2500 nm), a deuterium arc lamp which is continuous over the ultraviolet region (190-400 nm), and more recently light emitting diodes (LED) and Xenon Arc Lamp for the visible wavelengths. The detector is typically a photodiode or a CCD. Photodiodes are used with monochromators, which filter the light so that only light of a single wavelength reaches the detector. Diffraction gratings are used with CCDs, which collects light of different wavelengths on different pixels.

A spectrophotometer can be either *single beam* or *double* beam as shown in Fig.3.7. In a single beam instrument all of the light passes through the sample cell. I_o must be measured by removing the sample. This was the earliest design, but is still in common use in both teaching and industrial labs. In a double-beam instrument, the light is split into two beams before it reaches the sample. One beam is used as the reference; the other beam passes through the sample. Some double-beam instruments have two detectors (photodiodes), and the sample and reference beam are measured at the same time.

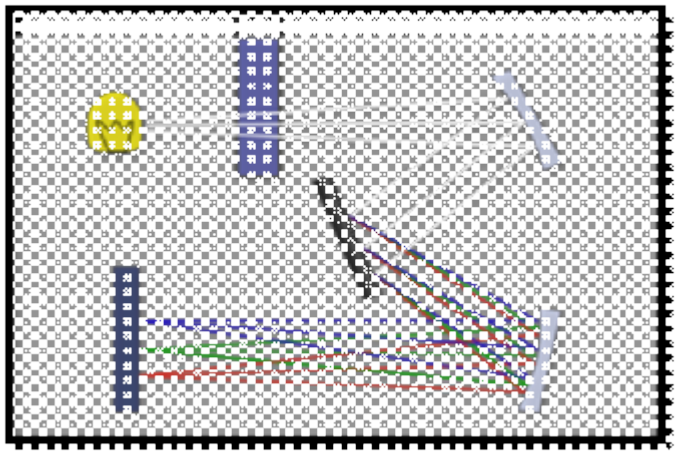

Fig.3.7 Single-beam UV/Vis spectrophotometer.

In other instruments, the two beams pass through a beam chopper, which blocks one beam at a time. The detector alternates between measuring the sample beam and the reference beam. Samples for UV/Vis spectrophotometry are most often liquids, although the absorbance of gases and even of solids can also be measured. Samples are typically placed in a transparent cell, known as a cuvette. Cuvettes are typically rectangular in shape, commonly with an internal width of 1 cm. (This width becomes the path length, *L*, in the Beer-Lambert law.) Test tubes can also be used as cuvettes in some instruments. The type of sample container used must allow radiation to pass over the spectral region of interest. The most widely applicable cuvettes are made of high quality fused silica or quartz glass because these are transparent throughout the UV, visible and near infrared regions. Glass and plastic cuvettes are also common, although glass and most plastics absorb in the UV, which limits their usefulness to visible wavelengths.

3.2.4) SCANNING ELECTRON MICROSCOPY:

Electron microscopy takes advantages of the wave nature of rapidly moving electrons. Where visible light has wavelengths from 4000 to 7000 angstroms, electron accelerated to 10,000 ev have a wavelength of 0.12 angstrom. Scanning electron microscope resolutions are currently limited to around 25 angstrom, through, for a variety of reasons. The scanning electron microscope generates a beam of electrons in the vacuum that beam is collimated by electromagnetic condenser lenses, focused by an objective lens, and scanned across the surface of the sample by electromagnetic deflection coils. The primary imaging method is

by collecting secondary electrons that are released by the sample. The scintillation material that produces flashes of the light from the electrons detects the secondary electrons. The light flashes are then detected and amplified by a photomultiplier tube. Fig.3.8 shows the image of a SEM

Fundamental Principles of Scanning Electron Microscopy (SEM)

Accelerated electrons in an SEM carry significant amounts of kinetic energy, and this energy is dissipated as a variety of signals produced by electron-sample interactions when the incident electrons are decelerated in the solid sample. These signals include secondary electrons (that produce SEM images), backscattered electrons (BSE), diffracted backscattered electrons (that are used to determine crystal structures and orientations of minerals), photons (characteristic X-rays that are used for elemental analysis and continuum X-rays), visible light (cathodoluminescence), and heat.

Fig.3.8 Scanning electron microscope

Secondary electrons and backscattered electrons are commonly used for imaging samples: secondary electrons are most valuable for showing morphology and topography on samples and backscattered electrons are most valuable for illustrating contrasts in composition in multiphase samples (i.e. for rapid phase discrimination). X-ray generation is produced by inelastic collisions of the incident electrons with electrons in discrete orbits (shells) of atoms in the sample. As the excited electrons return to lower energy states, they yield X-

rays that are of a fixed wavelength (that is related to the difference in energy levels of electrons in different shells for a given element).

3.2.5) FLUORESCENCE SPECTROSCOPY:

Fluorescence spectroscopy is a type of electromagnetic spectroscopy which analyzes fluorescence from a sample. It involves using a beam of light, usually ultraviolet light, that excites the electrons in molecules of certain compounds and causes them to emit light of a lower energy, typically, but not necessarily, visible light.

Theory and Instrumentation:

Molecules have various states referred to as energy levels. Fluorescence spectroscopy is primarily concerned with electronic and vibrational states. Generally, the species being examined has a ground electronic state (a low energy state) of interest, and an excited electronic state of higher energy. Within each of these electronic states are various vibrational states. In fluorescence spectroscopy, the species is first excited, by absorbing a photon, from its ground electronic state to one of the various vibrational states in the excited electronic state. Collisions with other molecules cause the excited molecule to lose vibrational energy until it reaches the lowest vibrational state of the excited electronic state. The molecule then drops down to one of the various vibrational levels of the ground electronic state again, emitting a photon in the process. As molecules may drop down into any of several vibrational levels in the ground state, the emitted photons will have different energies, and thus frequencies. Therefore, by analyzing the different frequencies of light emitted in fluorescent spectroscopy, along with their relative intensities, the structure of the different vibrational levels can be determined. In a typical experiment, the different wavelengths of fluorescent light emitted by a sample are measured using a monochromator, holding the excitation light at a constant wavelength. This is called an *emission spectrum.*

Two general types of instruments exist:

1) **Filter fluorometer**s use filters to isolate the incident light and fluorescent light.
2) **Spectrofluorometers** use diffraction grating monochromators to isolate the incident light and fluorescent light.

Both types utilize the following scheme: The light from an excitation source passes through a filter or monochromator, and strikes the sample. A proportion of the incident light is absorbed by the sample, and some of the molecules in the sample fluoresce. The fluorescent light is emitted in all directions. Some of this fluorescent light passes through a second filter or monochromator and reaches a detector, which is usually placed at 90° to the incident light beam to minimize the risk of transmitted or reflected incident light reaching the detector as shown in Fig.3.9.

Various light sources may be used as excitation sources, including lasers, photodiodes, and lamps; xenon arcs and mercury-vapor lamps in particular.

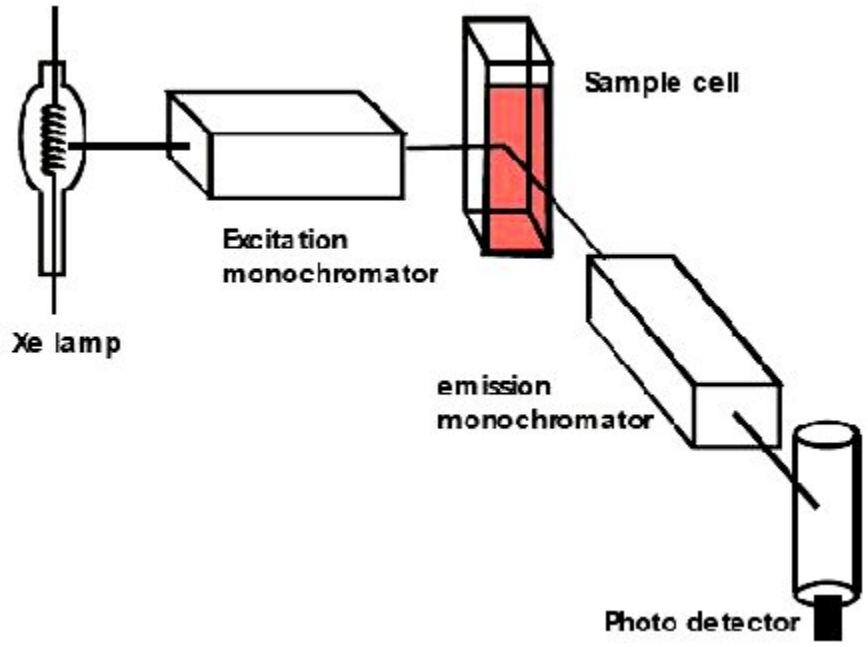

Fig.3.9 Working sequence of fluorescence spectrophotometer

Applications:

Fluorescence spectroscopy is used in, among others, biochemical, medical, and chemical research fields for analyzing organic compounds. There has also been a report of its use in differentiating malignant, bashful skin tumors from benign. Atomic Fluorescence Spectroscopy (AFS) techniques are useful in other kinds of analysis/measurement of a

compound present in air or water, or other media, such as CVAFS which is used for heavy metals detection, such as mercury.

3.2.6) DIELECTRIC MEASUREMENTS:

The properties of a piezoelectric ceramic are defined by piezoelectric, dielectric and elastic coefficients. All these are the functions of the state of polarization. They are amplitude dependent and become non linear or even non reversible when the applied signal or signal exceeds limits characteristics of the material. The dielectric and elastic coefficients have both real and imaginary part. Study of dielectric properties over a wide range of voltage and temperature is the principle tool for measuring ferroelectricity.

a) Low field measurements:

The low field dielectric constant ($K= \acute{\varepsilon}/\varepsilon_0$) and loss ($D=\varepsilon''/\acute{\varepsilon}$) of piezoelectric and ferroelectric ceramics are among their most important properties. Usually, these parameters are measured on electrode discs with the aid of well–engineered commercial instruments, such as Schering bridges, Q-meters, LCR meters as shown in Fig.3.10.

Fig.3.10 LCR meter

For good insulators, K does not vary much from dc to microwave frequencies. In ferroelectrics, especially in poled piezoelectric samples, there is a strong dependence of K on frequency. At low frequencies non uniform conductivity gives rise to interfacial

polarization which contributes to the effective dielectric constant and loss. Dipole relaxation connected with the impurities and domain wall motion also contribute to frequency dependence. A major and distinct contribution to frequency dependence of capacitance of poled ferroelectric ceramics is made by piezoelectric effect. In an unpoled sample of a ferroelectric ceramic, each domain acts as an individual partially constrained piezoelectric resonator. Typical domain dimension of 1μm place these elastic domain resonances into the 1000 MHz region where strong dispersion and dielectric loss are indeed observed.

b) High field measurement:

In poled samples of piezoelectric ceramics, high driving fields increase the effective dielectric constant and also caused increased loss. The increase of loss is important since the dielectrically generated heat may injure the transducer assembly or depole the ceramic.

Materials may be compared by measurements of K and D made at various field levels (frequently to ~ 10 Kv/cm) at frequencies below resonance under isothermal conditions. This is best accomplished by using thin specimens kept in a well-stirred oil bath. These measurements are typically made at 1000 Hz on small ceramic wafers. The connections are made directly to a LCR meter with no voltage divider or blocking capacitors. Materials vary widely in their dependence of K and D on driving field.

3.2.7) P-E LOOP MEASUREMENTS:

The polarization is the true measure of the degree of ferroelectricity. The polarization is the resultant of the dipole moments in each unit cell of a crystalline aggregate. In an unpoled ceramic, opposing moments cancel, but in a poled ceramic or a single domain crystal there is a net remanent polarization (P_r). Of interest also is the spontaneous polarization P_s obtained by extrapolating the polarization at fields P_{sat} back to zero field along the tangent. P_s is somewhat higher than P_r in ceramics. Generally, ceramics compositions with high values of P_r show usable piezoelectric effects. Polarization can be measured in number of ways including D/E hysteresis loops, pyroelectric depoling of a poled ceramic, pressure

depoling by extreme compression parallel to the poling direction with charge released into a short circuit.

The easiest, most frequently used approach is the investigation of charge-field hysteresis. Fig. 3.11 shows the typical hysteresis loop obtained in a ferroelectric ceramic. Briefly the method consists of applying an alternating voltage and relating the stored charge to the instantaneous voltage. A large integrating capacitor is placed in series with the sample and is conventionally displayed as the vertical deflection of an oscillograph. The applied field is displayed as the horizontal deflection. This arrangement works well for insulator samples, where substantially all the charges flowing are capacitive and are in phase with the driving voltage.

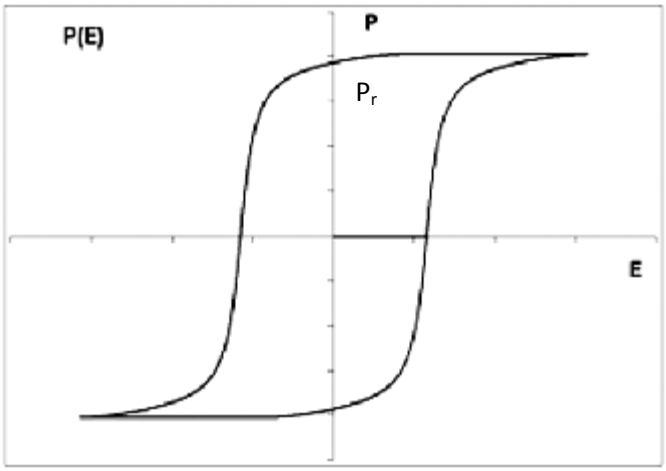

Fig. 3.11 Typical P-E loop

For non ferroelectric samples, a straight line results, while for a ferroelectric sample, a hysteresis loop is generated. The hysteresis arises from the energy needed to reverse the metastable dipoles during each excursion of the field. The area of the loop represents energy that is dissipated within the sample as heat. For this reason the experiment is usually run at low frequencies. Many ceramics are however, not good insulators; they conduct to some degree. The vertical deflection is then partially caused by dielectric displacement and partly by conduction. This conduction is either linear, that is, proportional to the field, or non linear as some power of the field. If we have a linear dielectric with linear conduction, the straight line changes to an ellipse and we speak of it as that of a lossy linear capacitor. If we have a non linear ferroelectric with linear conductivity, its hysteresis loop is the resultant of the two effects. In such a case, it is legitimate to shift the phase of the voltage so that the phase

difference caused by the conduction is cancelled. This can be done by inserting a variable resistor. In practice, the variable resistor can be either in series or parallel with any of the four capacitive elements, yet have the same phase shifting effect if its value is properly adjusted. A true ferroelectric has true dielectric hysteresis; it also has generally a dielectric constant peak at a Curie point, domain structure, bifringence and a high dielectric constant. Fig.3.12 displays the image of a P-E loop tracer system.

Fig.3.12 P-E loop tracer system

CHAPTER 4

RESULTS AND DISCUSSION

This chapter contains results obtained from X-Ray Diffraction (XRD), Fourier Infra Red Spectroscopy (FTIR), U.V- Visible Spectroscopy, Fluorescence Spectroscopy, Dielectric and P-E loop characterizations and their analysis to understand structural, chemical, optical, morphological, dielectric and ferroelectric behavior of synthesized pure and doped ZnO.

4.1) STRUCTURAL ANALYSIS:

The structural analysis of the as prepared pure and modified ZnO has been investigated using X-Ray diffraction method (Cu K_α radiations of wavelength= 1.54 A^0, Philips X'pert Pro) at room temperature.

4.1.1) X-Ray diffraction Pattern of Pure and Samarium doped ZnO:

The XRD patterns of the Commercial available, Synthesized and Samarium doped ZnO are shown in Fig.4.1. Highly intense peaks extended over 2θ scale infer about the crystalline nature of the material in pure and doped sample.

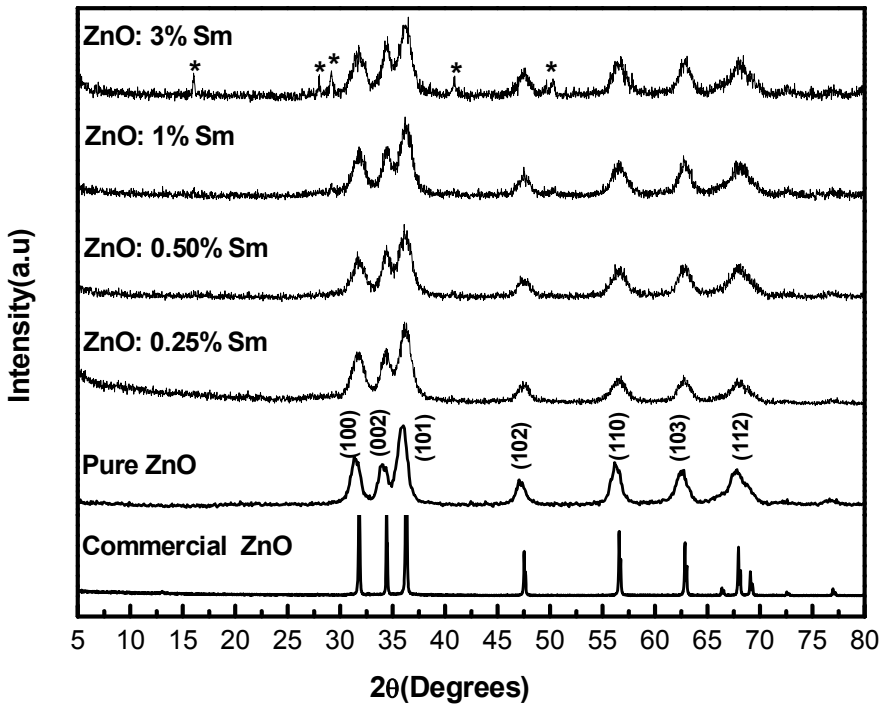

Fig.4.1 XRD patterns of Commercial available, Synthesized and Samarium doped ZnO

The peaks observed at $2\theta=31.5^0$, 33.92^0, 35.93^0, 47.18^0, 56.20^0, 62.73^0, 67.37^0 correspondence to the lattice plane (100), (002), (101), (102), (110), (103) and (112) respectively, indicative of wurtzite hexagonal structure of ZnO. All the peaks are matched with standard JCPDS card no. 50664.

From the XRD pattern it is clear that at higher doping of 3% pure phase has not been achieved. However, as the dopant concentration reached 3% the ZnO phase has been achieved along with extra peaks marked as * in the Fig.4.1, which infer that at higher concentration (3%) dopant are not occupying the valence site and randomly oriented in the sample.

Broadening in peaks appeared for the XRD pattern of synthesized ZnO that of commercial available bulk ZnO inferring about the smaller crystallite size. A modified form of Debye Scherer formula has been used for the calculation of the average particle size (T)

$$T = \frac{0.9\,\lambda}{cos(\theta)} (\beta_0^2-\beta_a^2)^{-1/2} \quad \text{.....(1)}$$

Where, β_0 = FWHM of the diffraction peak for the synthesized sample.

β_a = FWHM of the diffraction peak for commercial available sample.

θ = Angle corresponding to the diffraction peak.

λ = Wavelength of the X ray used.

The average particle size calculated using above formula for (101) peak has been listed below in Table.4.1

Table 4.1 Average particle size for Samarium doping

S.No	Material	Average particle size (nm)
1.	Pure ZnO	7
2.	ZnO: 0.25% Sm	9
3.	ZnO: 0.50 % Sm	16
4.	ZnO: 1% Sm	10

The variation of average particle size with the doping concentration of samarium has been shown graphically in Fig (4.2). It is quite clear that the particle size of doped ZnO is more than that of pure ZnO.

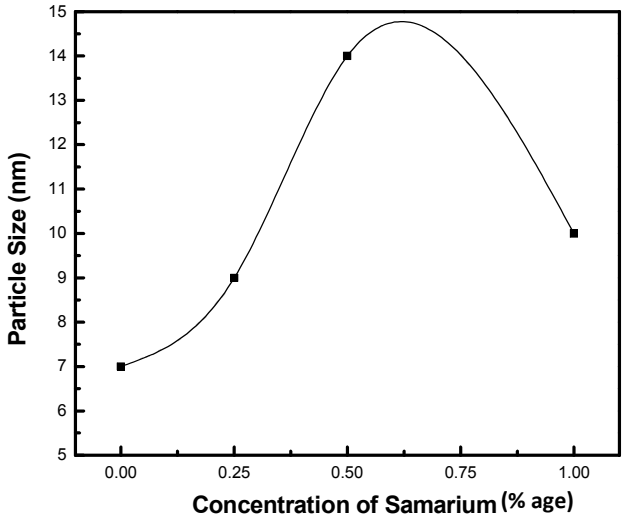

Fig.4.2 Variation of Particle Size with samarium concentration

The lattice constants for commercial available, synthesized and doped ZnO has been calculated from the formula given below in eqn. 2.

$$\frac{1}{d^2} = \frac{4}{3}\left(\frac{h^2+k^2+hk}{a^2}\right) + \frac{l^2}{c^2} \quad \text{.....(2)}$$

Where, **d** = inter planner spacing, ***h,k,l*** = Miller indices of the plane and **a,c** = lattice constants.

The values of lattice constants calculated from this formula have been tabulated in Table 4.2. From the above analysis it can be concluded that the value of lattice constants **'a'** and **'c'** changes with the doping, which reflects that Zn atoms are being replaced by the samarium atoms. The variation of lattice constants as a function of samarium doping is shown in the Fig.4.3.

Table 4.2 lattice constants of commercial available, synthesized and Samarium doped ZnO

S.No	Material	**a** (A^0)	**c** (A^0)	c/a
1.	Commercial ZnO	3.2520	5.2109	1.6023
2.	Pure ZnO	3.2754	5.2844	1.6133
3.	ZnO: 0.25% Sm	3.2690	5.2178	1.5961
4.	ZnO: 0.50 % Sm	3.2753	5.2230	1.5946
5.	ZnO: 1% Sm	3.2417	5.1965	1.6030

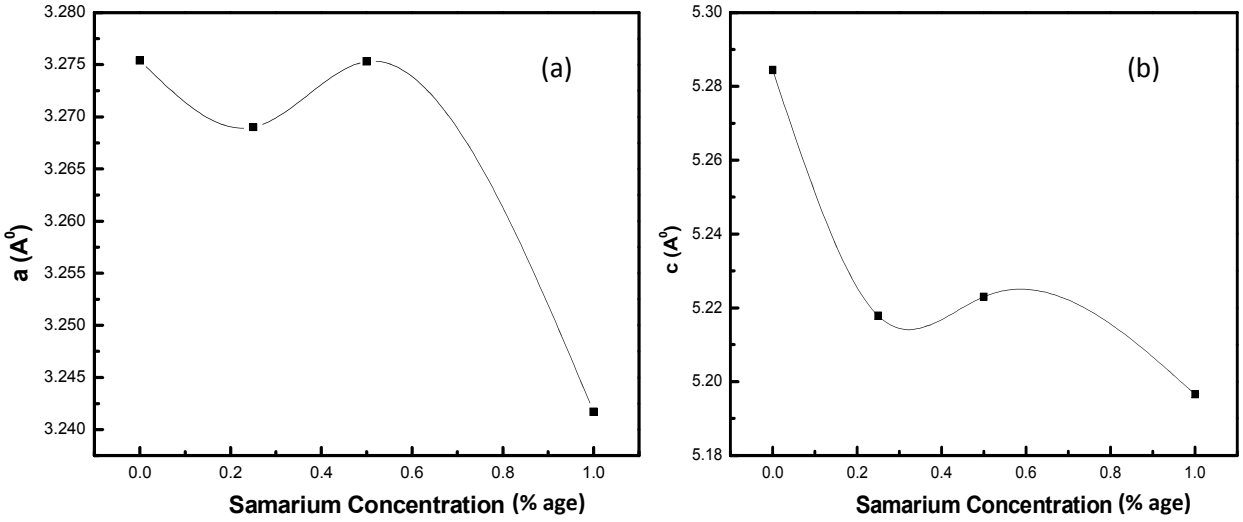

Fig.4.3 Variation of Lattice constants with concentration (a) **'a'** (b) **'c'**

From the graphs, it is clear that with the addition of Samarium ion the value of lattice constants decrease that of pure ZnO, this is because of the higher charge of Samarium (+3) as compare to Zinc (+2), as consequence of which oxygen atoms are attracted more towards Samarium this produces contraction in lattice. Moreover, c/a ratio for the Samarium doped ZnO is lower than that of synthesized pure ZnO, which reveals the decrease in the lattice distortions and hence confirming the substitution of Samarium at Zn site.

4.1.2) X-Ray diffraction Pattern of Europium doped ZnO:

Fig.4.4 displays the diffractrograms of Europium doped ZnO. All the peaks of the XRD pattern were indexed with standard JCPDS card no. 50664 confirming wurtzite hexagonal crystal structure.

The XRD pattern reveals a successful doping of Europium up to 3% as no extra peaks were observed up to 3% Europium content.

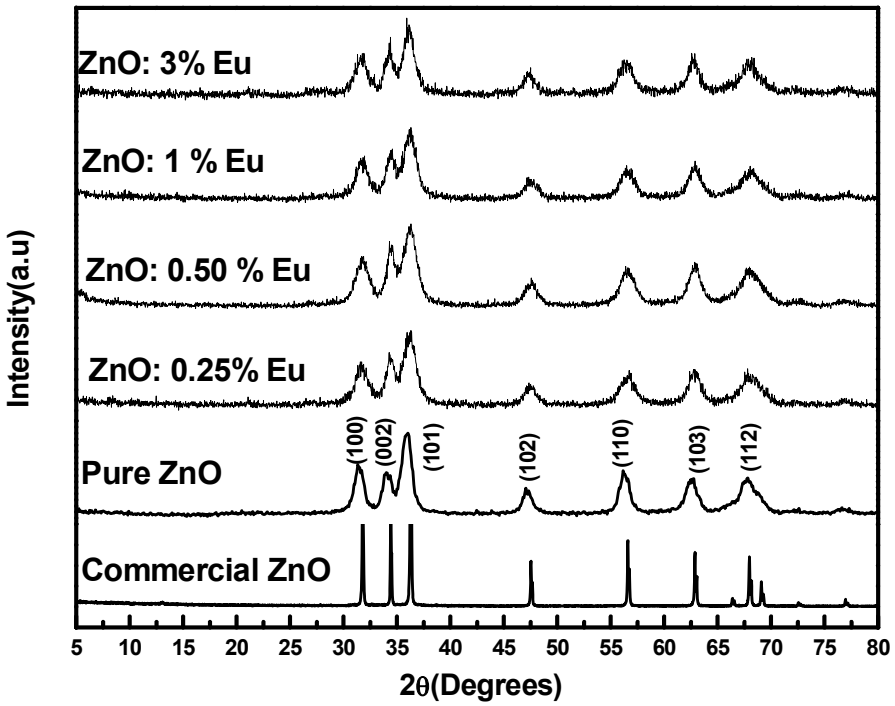

Fig.4.4 XRD patterns of Europium doped ZnO

Broadening in the peaks of the XRD patterns clearly shows the reduction in crystallite size. The particle size for (101) peak was calculated using of eqn. 1 and tabulated below in Table 4.3.

Table 4.3 Average particle size for Europium doping

S.No	Material	Average particle size (nm)
1.	Pure ZnO	7
2.	ZnO: 0.25% Eu	8
3.	ZnO: 0.50 % Eu	24
4.	ZnO: 1% Eu	16
5.	ZnO: 3% Eu	9

The particle size variation with increasing concentration of Europium has been shown graphically in Fig.4.5. It was found that particle size is increased up to 0.5% Europium doping and then decline to lower value at higher concentrations though the magnitude remains higher for doped case than that of pure one.

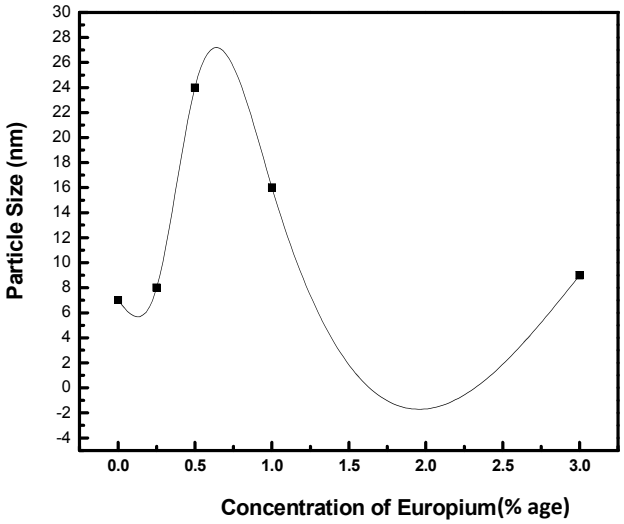

Fig.4.5 Particle Size variation with Europium concentration

Lattice constants for the Europium doping are calculated by making use of eqn. 2 and are tabulated in Table 4.4.

Table 4.4 lattice constants Europium doped ZnO

S.No	**Material**	**a** (A^0)	**c** (A^0)	**c/a**
1.	Commercial ZnO	3.2520	5.2109	1.6023
2.	Pure ZnO	3.2754	5.2844	1.6133
3.	ZnO: 0.25% Eu	3.2676	5.2193	1.5972
4.	ZnO: 0.50 % Eu	3.2479	5.2113	1.6045
5.	ZnO: 1% Eu	3.2479	5.2127	1.6049
6.	ZnO: 3% Eu	3.2396	5.2241	1.6125

Small change in the lattice constants has been observed with the Europium doping, which gives an inference about the replacement of Zinc atoms with Europium atoms. The variation of the lattice constants with the Europium concentration is shown in the Fig (4.6). The behavior obtained in Fig.4.6a and Fig.4.6b indicates that addition of Europium into the Zn site the value of lattice constants shift to lower magnitudes which is attributed to higher charge on Europium as compare to Zinc, as evident from Fig.4.6a and Fig.4.6b that the value of 'a' decreased with increasing concentration of Europium, conversely the value of 'c' found to be increased fro same dopant concentrations, this is because of the ionic size of

Europium is quite large as compare to Zinc and as the doping concentration is increased more number of Europium atoms replace Zinc atoms and hence indicating small increment in the 'c' value.

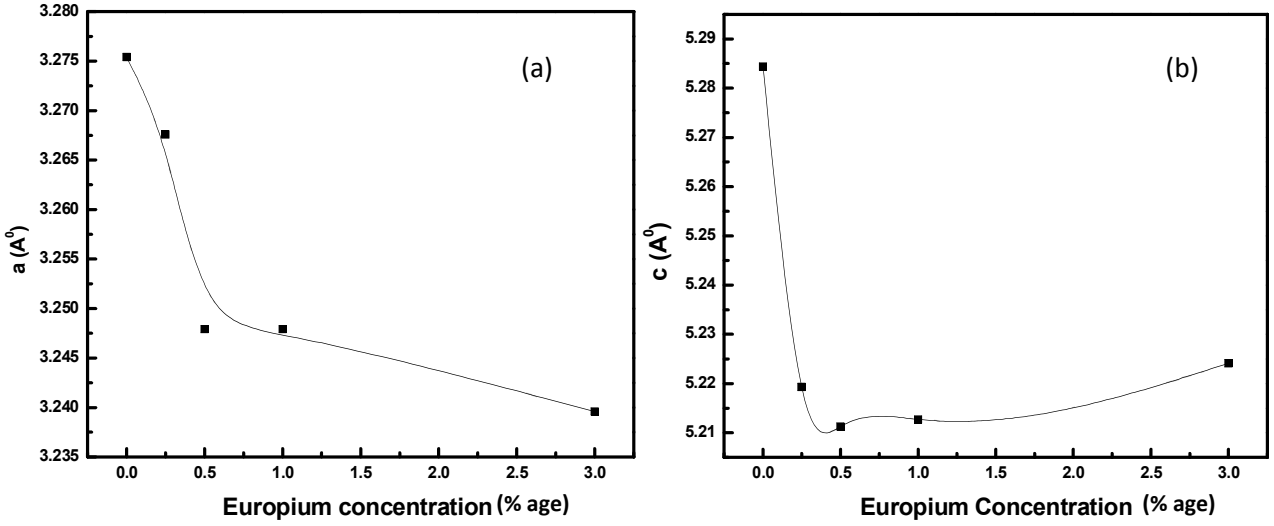

Fig.4.6 Variation of Lattice constants with concentration (a) 'a' (b) 'c'

Moreover, the c/a ratio in the Europium doped ZnO comes out to be lesser as compare to pure ZnO which reveals the reduction in lattice distortions. The reduction in lattice distortion confirms an efficient doping of Europium in ZnO lattice without disturbing the symmetry of the wurtzite hexagonal structure.

4.1.3) X-Ray diffraction Pattern of Titanium doped ZnO:

The XRD patterns of Titanium doped ZnO powders are presented in Fig .4.7. Diffraction peaks observed for these systems are well indexed with standard JCPDS card no. 50664. All these patterns confirm the formation of wurtzite hexagonal structure. It is evident from Fig.4.7 that Titanium dopant occupies the valence site up to 3% concentration, as no impurity peak has been appeared in XRD pattern.

The formation of small particles is being confirmed by the broadening in the XRD peaks, which further calculated by using of eqn. 1 for (101) plane and listed in the Table 4.5.

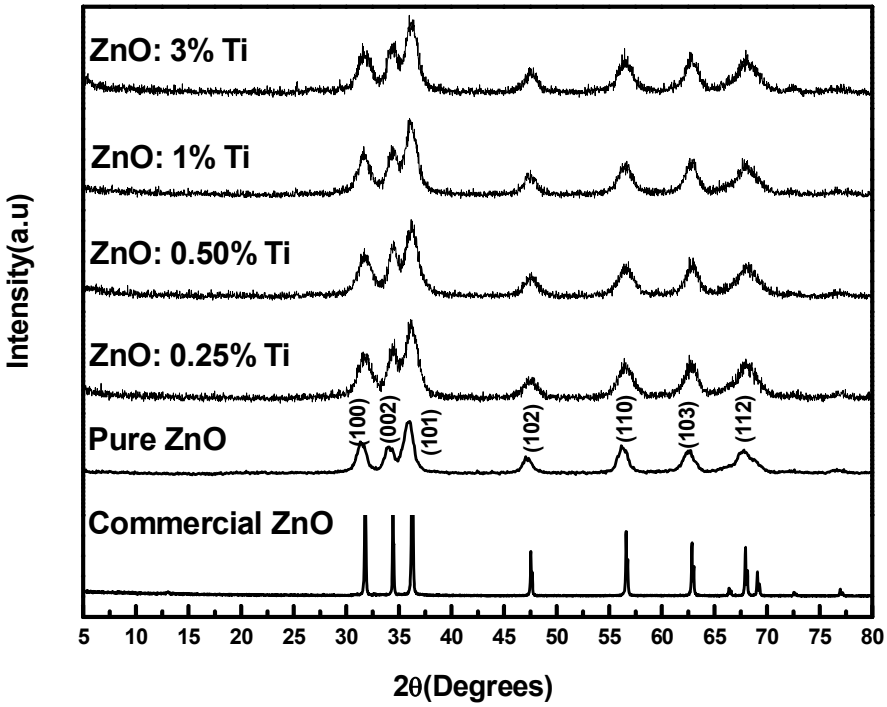

Fig.4.7 XRD pattern of Titanium doped ZnO

Table 4.5 Average particle size of Titanium doped ZnO

S.No	Material	Average particle size (nm)
1.	Pure ZnO	7
2.	ZnO: 0.25% Ti	14
3.	ZnO: 0.50 % Ti	12
4.	ZnO: 1% Ti	14
5.	ZnO: 3% Ti	20

The variation in the particle size for Titanium doped ZnO is shown graphically as in Fig.4.8. It was found that the doping of Ti ion increasing the particle size up to higher concentrations.

Lattice constants for Titanium doped ZnO has been used calculated using eqn. 2 and are listed in Table 4.6.

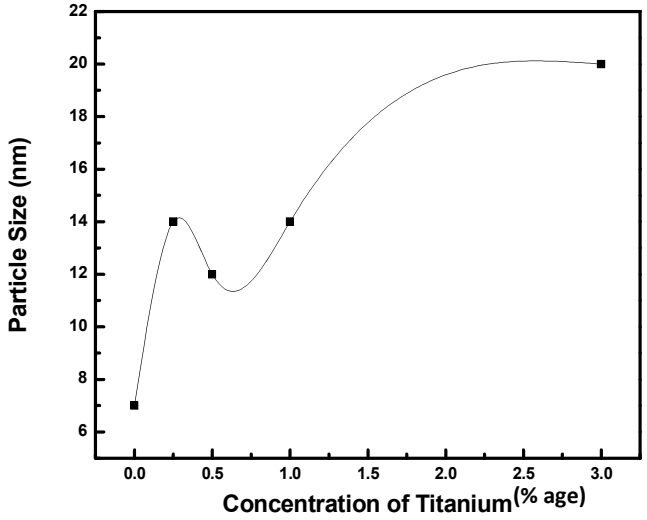

Fig.4.8 Variation of particle size with Titanium concentration

Table 4.6 lattice constants of Titanium doped ZnO

S.No	Material	a (A^0)	c (A^0)	c/a
1.	Commercial ZnO	3.2520	5.2109	1.6023
2.	Pure ZnO	3.2754	5.2844	1.6133
3.	ZnO: 0.25% Ti	3.2681	5.1944	1.5894
4.	ZnO: 0.50 % Ti	3.2710	5.1967	1.5887
5.	ZnO: 1% Ti	3.2718	5.2088	1.5920
6.	ZnO: 3% Ti	3.2908	5.2646	1.5997

The above analysis conveys that doping of Titanium has its effect on the values of lattice constants ‘a’ and ‘c’ and they change with the doping of Titanium. Therefore, we can say that Titanium substitutes at the Zinc site. The variation of the lattice constants with the concentration of Ti has been shown in the Fig.4.9.

We observed that lattice constants ‘a’ and ‘c’ at 0.25% concentration of Ti ion are found decreased and then gradually increased with the rise in dopant concentration. Note that the value of ‘a’ become higher than that of pure ZnO at 3% concentration, however the value of ‘c’ remains a bit lower than the pure ZnO. Such behavior of these Titanium doped samples attributed to the higher charge of Titanium ion, which plays an important role at lower concentration as evident from Fig.4.9a and Fig.4.9b. But as the concentration is increased, the number of Titanium ions accumulation at Zinc site becomes more. Thus resulting enhancement in ‘a’ and ‘c’ values. Such behavior may be attributed to the ionic

radii which is higher than that of Zinc ion. The reduced c/a ratio gives an indication of the reduction in lattice distortion, which in turns confirms the doping of Titanium at the valence site of Zinc.

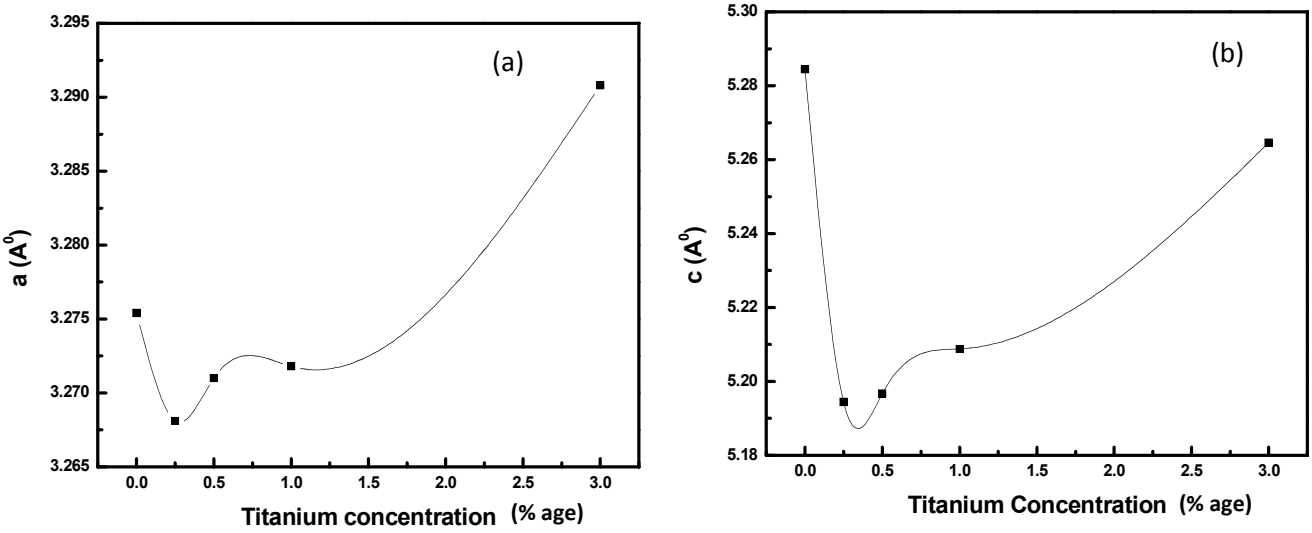

Fig.4.9 Variation of Lattice constants with concentration (a) 'a' (b) 'c'

4.1.4) X-Ray diffraction Pattern of Niobium doped ZnO:

The XRD pattern of Niobium doped ZnO is shown in Fig.4.10.

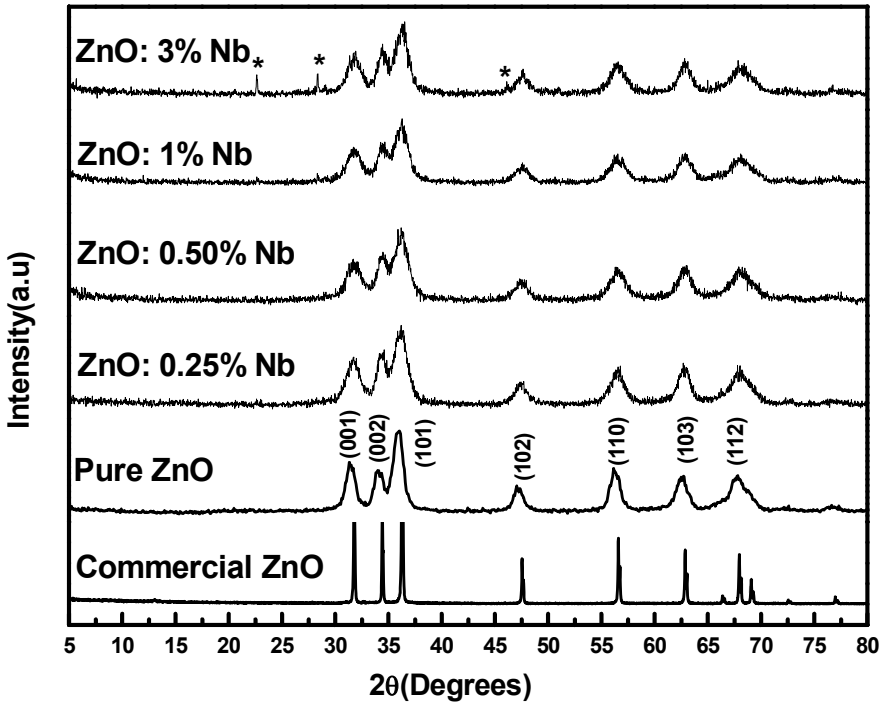

Fig.4.10 XRD patterns of Niobium doped ZnO

From the diffractrograms obtained for Niobium doped ZnO it is quite clear that up to 1% Niobium concentration the diffraction lines are characteristics of wurtzite hexagonal structure, no extra peak was found, which indicates that Niobium has induced in the ZnO lattice without changing the wurtzite structure. However, at 3% concentration of Niobium peaks marked as * appears in the diffractrogram, which confirms appearance of mixed phase of Nb_2O_5 and ZnO, which indicates Nb_2O_5 does not get hydrolyzed at higher concentrations (3%) and remains unreacted in the reaction.

The particle size for different Niobium concentration corresponding to (101) peak has been calculated using eqn. 1 and are listed in Table 4.7.

Table 4.7 Average particle size of Niobium doped ZnO

S.No	Material	Average particle size (nm)
1.	Pure ZnO	7
2.	ZnO: 0.25% Nb	14
3.	ZnO: 0.50 % Nb	9
4.	ZnO: 1% Nb	10

The variation of the particle size as a function of concentration is shown graphically in Fig.4.11. It is observed from the graph that particle size increase at 0.25% concentration and then decrease to lower value at higher concentration, though the magnitude is still higher than that of pure ZnO.

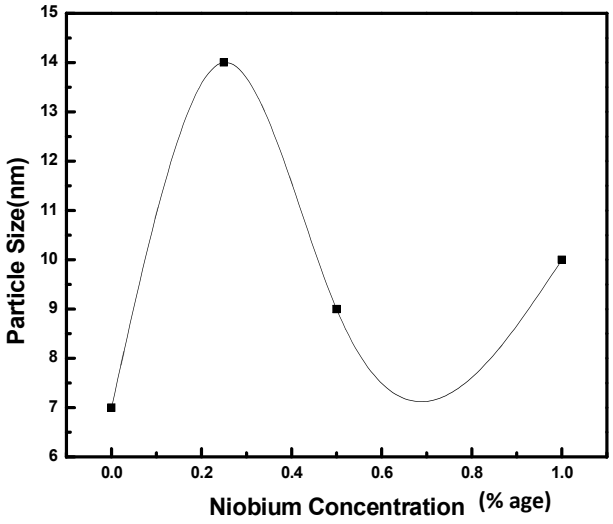

Fig.4.11 Variation of Particle size with Niobium concentration

The lattice constants for Niobium doped ZnO are calculated by employing eqn. 2 and are listed in Table 4.8.

Table 4.8 Lattice constants of Niobium doped ZnO

S.No	Material	**a** (A^0)	**c** (A^0)	c/a
1.	Commercial ZnO	3.2520	5.2109	1.6023
2.	Pure ZnO	3.2754	5.2844	1.6133
3.	ZnO: 0.25% Nb	3.2269	5.1912	1.6087
4.	ZnO: 0.50 % Nb	3.2441	5.2190	1.6087
5.	ZnO: 1% Nb	3.2629	5.2389	1.6055

From the above data it is clear that that doping of Niobium has a strong influence on the lattice constants values, which in turns gives evidence for the replacement of Zinc atom with the Niobium atom. From the graph it is quite clear that the values of lattice constants of doped ZnO are less than that of pure ZnO. The variation of the lattice constants with the concentration of the Niobium is shown graphically in Fig.4.12.

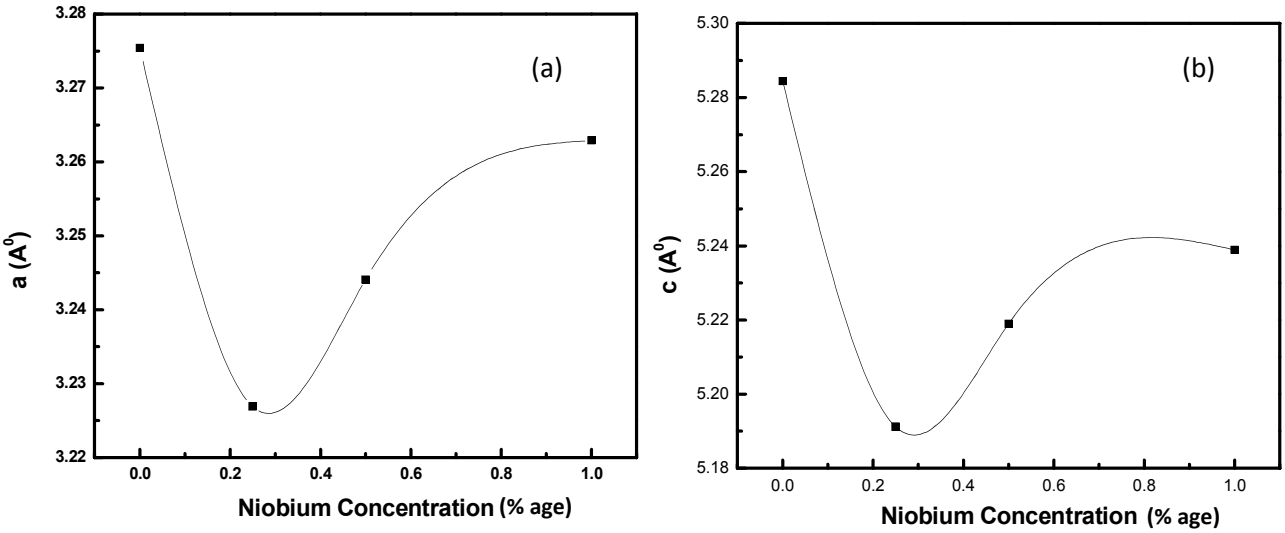

Fig (4.12) Variation of Lattice constants with concentration (a) 'a' (b) 'c'

The values of the lattice constants in general increase with the Niobium concentration, this is due to the reason that the size of Niobium ion is larger than that of Zn and as the doping is increased the number of Niobium atoms in the ZnO lattice increases and hence the lattice constants increased with the doping of Niobium.

Also the **c/a** ratio for the Niobium doping is less as compare to that of pure ZnO, which gives an idea of lattice contraction and reduction in lattice distortion which then account for efficient doping of Niobium at Zn site.

4.2) CHEMICAL ANALYSIS:

The Chemical analysis of the as prepared pure and modified ZnO has been investigated using Fourier Transform Infra Red Spectroscopy (Perkin Elmer Spectrum BX II) in range of wave number 400 to 4000 cm^{-1}.

4.2.1) FTIR spectrum of pure and Samarium doped ZnO:

The FTIR spectrum of the pure and Samarium doped ZnO is shown in the Fig.4.13.

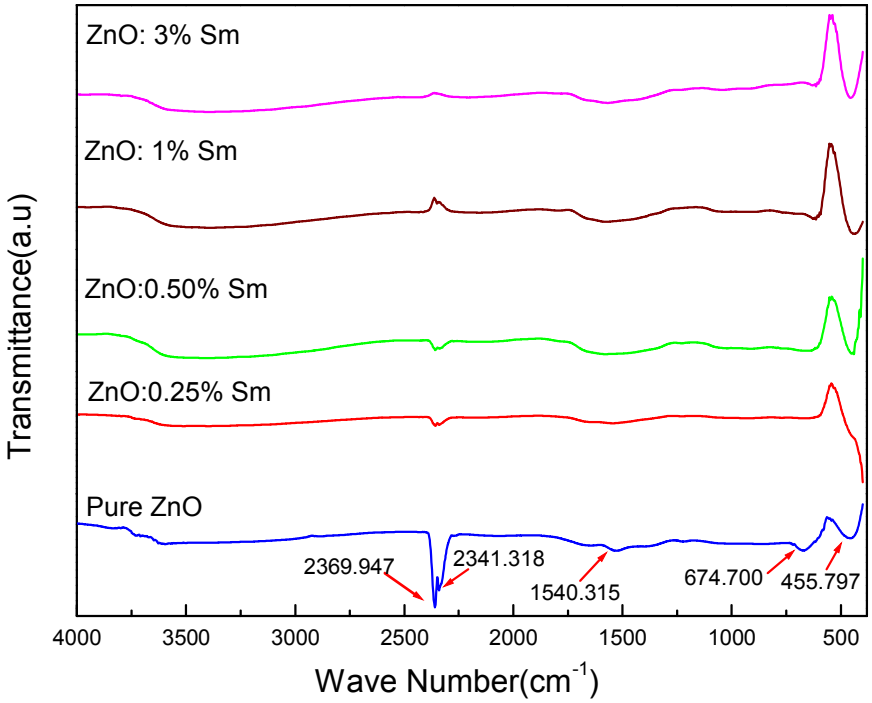

Fig.4.13 FTIR spectrum of the pure and Samarium doped ZnO

Peak obtained at 455.797 cm^{-1}, indicates the formation of Zn-O bond in the sample. The reflections at 2369.947cm^{-1} and 2341.3183cm^{-1} represents the presence of C-H bond. Furthermore, small peaks obtained at 1540.315 cm^{-1} and 674cm^{-1} are due to the presence of COO^- and cis-di substituted alkenes. The peaks except 455.797 cm^{-1} can be removed easily by heating. Also, with the addition of Samarium no extra peak in the spectrum has been obtained which indicates the absence of other phase additives in the sample and ZnO is free

from complexes. The FTIR spectrum gives preliminary information about the ZnO phase formation which is in good agreement with the XRD analysis.

4.2.2) FTIR spectrum of pure and Europium doped ZnO

The FTIR spectrum of the pure and Europium doped ZnO is shown in the Fig.4.14.

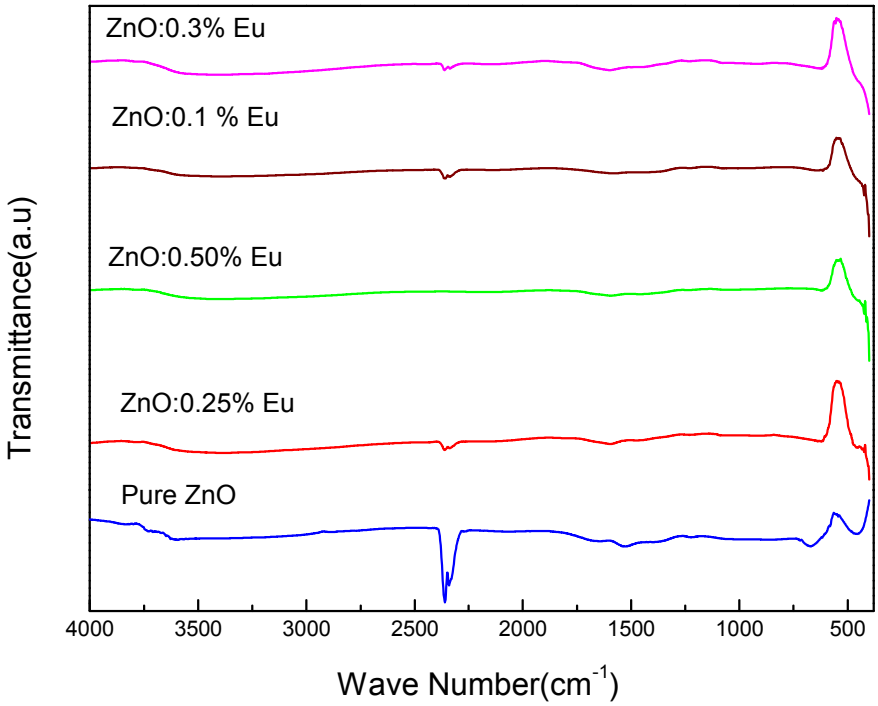

Fig.4.14 FTIR spectrum of the pure and Europium doped ZnO

The above spectrum indicates the formation of Zn-O in Europium doped sample without any extra peak obtained, which reflects that dopant are bond to Zinc site, no other bond of Eu-O has been observed.

4.2.3) FTIR spectrum of pure and Titanium doped ZnO:

The FTIR spectrum of the pure and Titanium doped ZnO is shown in the Fig.4.15. From spectra it is clear that the peaks at 455.797 cm^{-1} corresponds to formation of Zn-O bond in the pure as well as in the Titanium doped ZnO. No other Ti-O bond has been seen in the spectra. The FTIR spectrum gives preliminary information about the ZnO phase formation which is in good agreement with the XRD analysis.

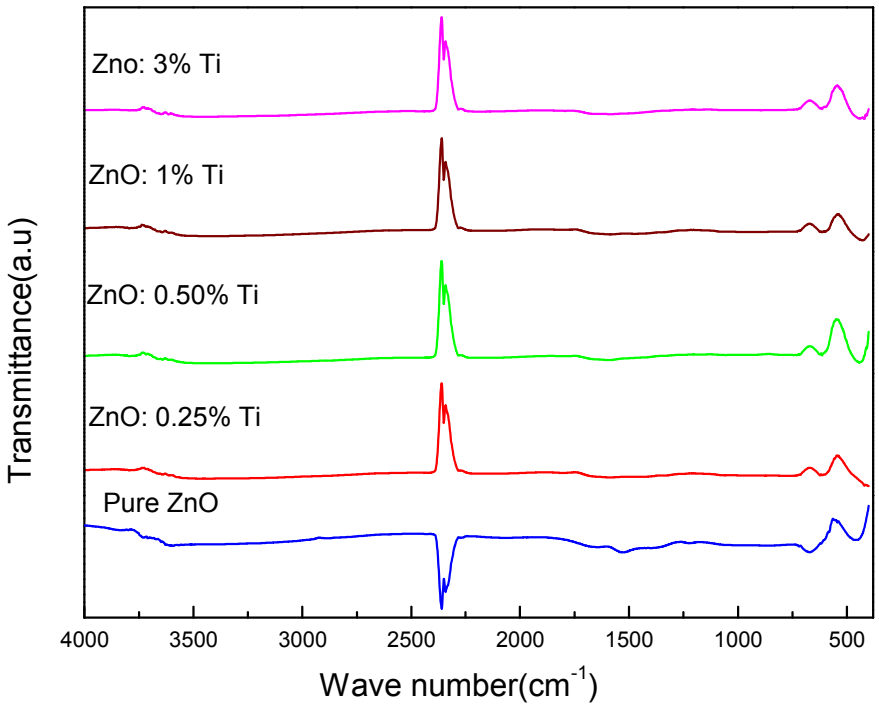

Fig.4.15 FTIR spectrum of the pure and Titanium doped ZnO

4.2.4) FTIR spectrum of pure and Niobium doped ZnO:

The FTIR spectrum of the pure and Niobium doped ZnO is shown in the Fig.4.16

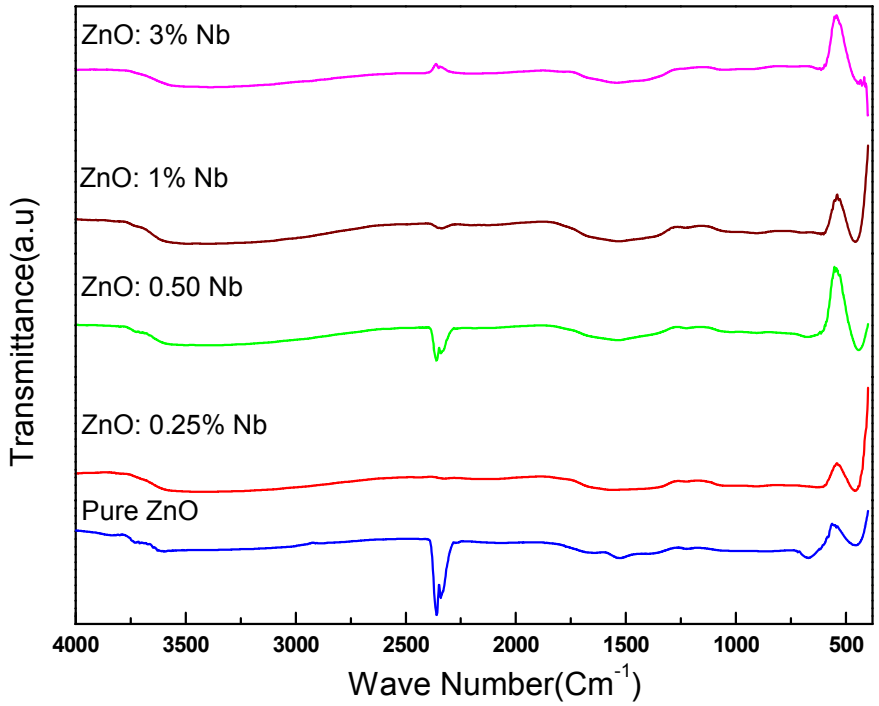

Fig.4.16 FTIR spectrum of the pure and Niobium doped ZnO

From the IR spectra it is clear that Zn-O bond has been formed in the Niobium doped ZnO. No other bond of parent precursor and dopant was found in these samples.

4.3) OPTICAL ANALYSIS:

The optical properties of pure and modified ZnO have been investigated by using UV-vis (Lambda 25 Perkin Elmer) spectrophotometer and photoluminescence properties are investigated by fluorescence spectrophotometer (Cary Eclipse fluorescence spectrophotometer) to understand optical behavior of the doped samples.

4.3.1) UV –Vis SPECTRA OF PURE AND SAMARIUM DOPED ZnO:

The UV-Vis spectra of pure ZnO and Samarium doped ZnO is shown in Fig.4.17.

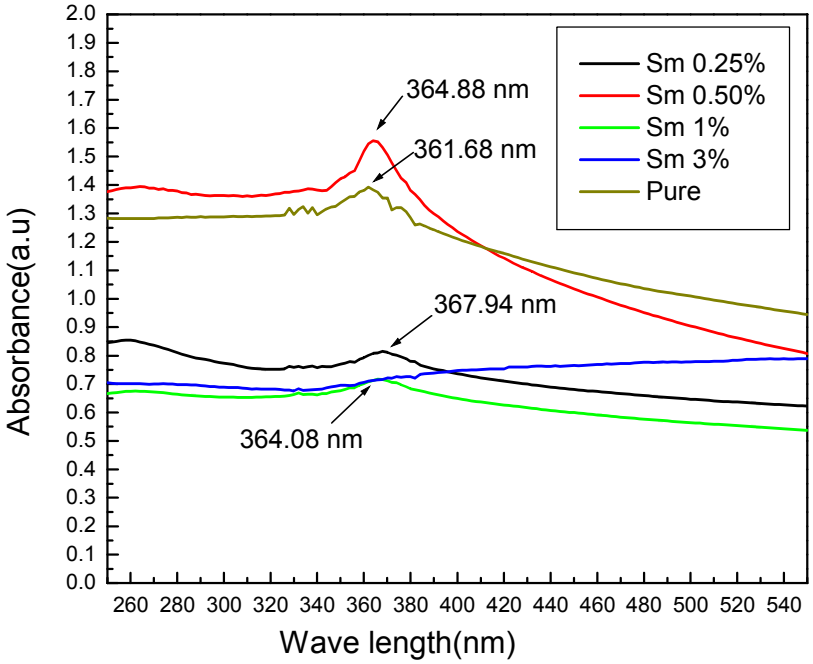

Fig.4.17 UV-Vis spectra of pure ZnO and Samarium doped ZnO

From the literature, the exciton absorption of pure ZnO is at 380 nm corresponds to a band gap of 3.26 eV (as calculated by $E=\frac{hc}{\lambda}$). The spectra obtained for the pure ZnO reveals that the exciton absorption of pure ZnO is at 361.68 nm which corresponds to a band gap of 3.428 eV and represent blueshift (18 nm). This result clearly reflects that the band gap of pure ZnO has been increased which may be due to decrease in crystallite size. There is an increase in band gap of material at nanoscale because at this level the particle size becomes

smaller than the Bohr radius of the exciton and thus so called quantum size effect takes place. As a result of these quantum size effects, at the edges of the valence and conduction band discrete energy levels occur and thus the band gap increases.

With the addition of the Samarium in the pure ZnO the absorption peak get shifted to higher side of wavelength. At 0.25% Samarium the absorption peak is at 367.94 nm which corresponds to a band gap of 3.36 eV. As the dopant concentration is increased absorption peak again shift to lower wavelength such behavior reveals that samarium has introduced trapped levels in the forbidden gap and the absorption takes from these levels which lower the band gap. With the further increase in the doping the band gap increases. At 3% samarium no definite absorption peak is obtained, this is because at 3% Samarium concentration a mixed phase of Sm_2O_3 and ZnO has been obtained. The values of band gap and corresponding absorption peaks are listed in Table 4.9.

Table 4.9 Band gap of pure and Samarium doped ZnO

Material	**Absorption Peak (nm)**	**Calculated Band gap (eV)**
Pure ZnO	361.68	3.428
0.25% Samarium	367.93	3.369
0.50% Samarium	364.88	3.398
1% Samarium	364.08	3.405

4.3.2) UV –Vis SPECTRA OF PURE AND EUROPIUM DOPED ZnO:

The UV-Vis spectra of pure ZnO and Europium doped ZnO is shown in Fig.4.18. From the spectra it is clear that at 0.25% concentration of Europium, the absorption peak was obtained at 373.41 nm which corresponds to a band gap of 3.320 eV. This decrease in the band gap is because of the formation of trapped levels in the forbidden gap. A regular shift towards the lower wavelength in the peaks is observed with increasing the Europium concentration, which consequently indicating an increase in band gap with increasing the doping concentration. The band gap and the absorption peaks for the different dopant concentration has been tabulated in Table.4.10.

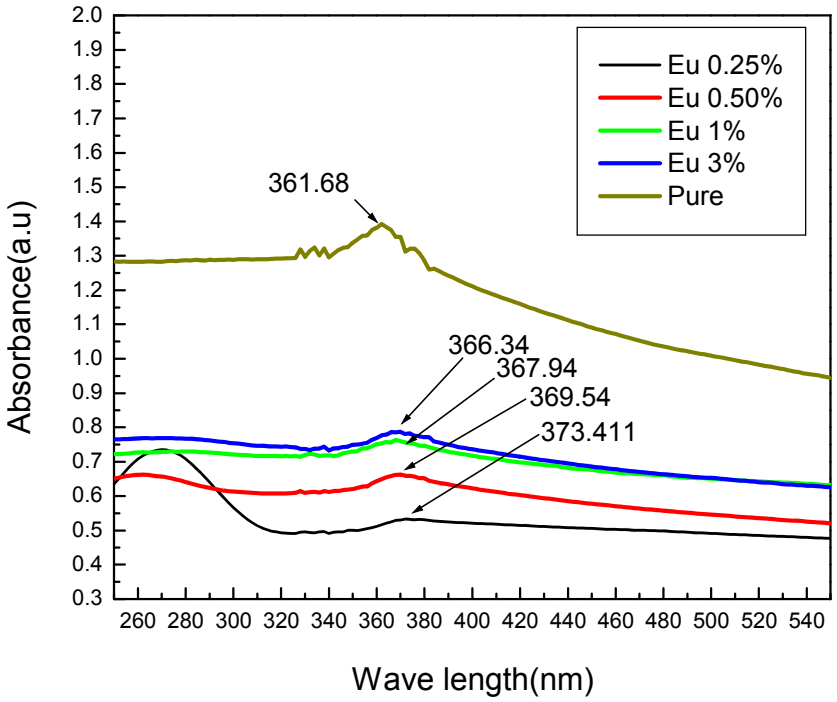

Fig.4.18 UV-Vis spectra of pure ZnO and Europium doped ZnO

Table 4.10 Band gap of pure and Europium doped ZnO

Material	Absorption Peak (nm)	Calculated Band gap (eV)
Pure ZnO	361.68	3.428
0.25%	373.41	3.320
0.50%	369.54	3.355
1%	367.94	3.37
3%	366.34	3.384

4.3.3) UV –Vis SPECTRA OF PURE AND TITANIUM DOPED ZnO:

The UV-Vis spectra of pure ZnO and Titanium doped ZnO is presented in Fig.4.19. From the spectra it is clear that when Titanium is introduced into the ZnO lattice then it creates impurities levels in the energy gap due to which the band gap decreased. In the case of Titanium doping the band gap decreases with the increasing Titanium concentration, this is due to increase in the number of impurity states with increasing Titanium concentration. The values of absorption peaks and band gap has been listed in Table.4.11.

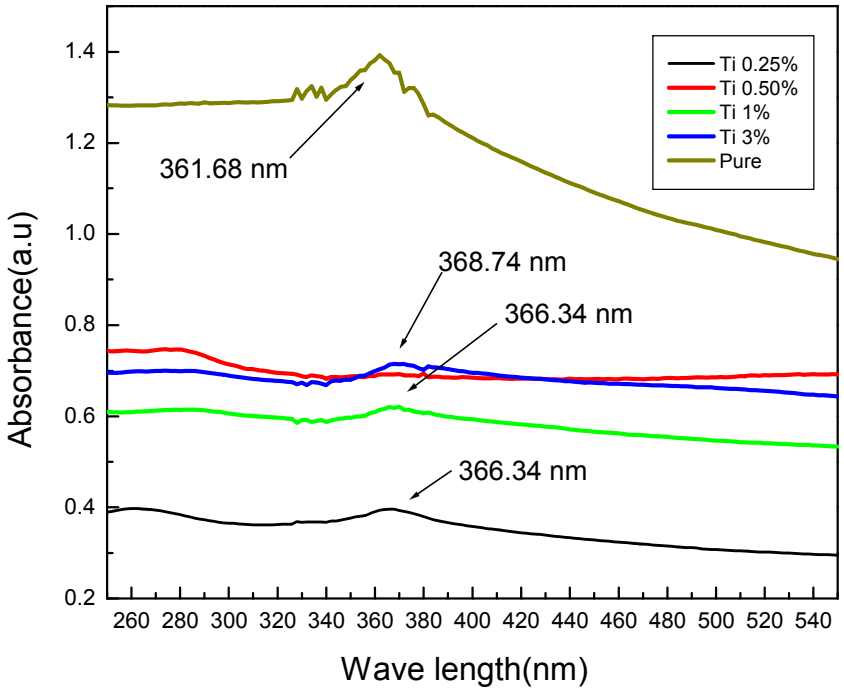

Fig.4.19 UV-Vis spectra of pure ZnO and Titanium doped ZnO

Table 4.11 Band gap of pure and Titanium doped ZnO

Material	**Absorption Peak (nm)**	**Calculated Band gap (eV)**
Pure ZnO	361.68	3.428
0.25%	366.34	3.38
0.50%	No sharp peak	……..
1%	366.34	3.38
3%	368.74	3.362

4.3.4) UV –Vis SPECTRA OF PURE AND NIOBIUM DOPED ZnO:

The UV-Vis spectra of pure ZnO and Niobium doped ZnO is shown in Fig.4.20. From the spectra it is clear that Niobium doping also influence the band gap of ZnO. As Niobium ion was added to ZnO lattice it introduces its impurity states in the energy gap and therefore band gap decrease. The values of absorption peaks and calculated band gap are listed in Table.4.12.

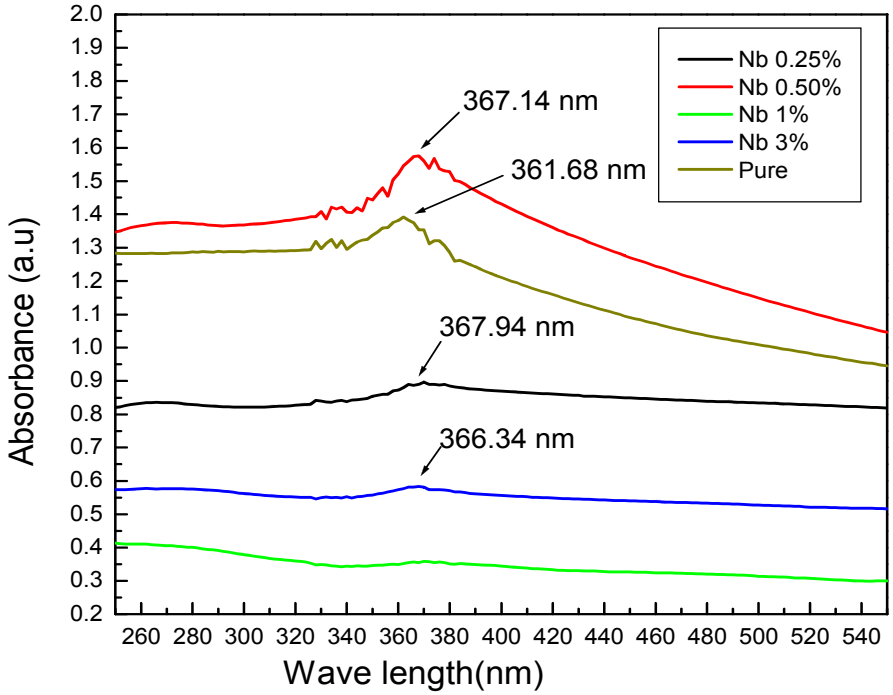

Fig.4.20 UV-Vis spectra of pure ZnO and Niobium doped ZnO

Table 4.12 Band gap of pure and Niobium doped ZnO

Material	**Absorption Peak (nm)**	**Calculated Band gap (eV)**
Pure ZnO	361.68	3.428
0.25%	367.94	3.37
0.50%	367.14	3.35
1%	No Sharp peak	……

4.3.5) PHOTOLUMINESCENCE SPECTRA OF PURE AND EUROPIUM DOPED ZnO:

The photoluminescence of the pure and the Europium doped ZnO has been investigated by using photoluminescence fluorescence spectroscopy at different excitation wavelengths. Fig. 4.21 demonstrates the PL spectra of pure and Europium doped ZnO.

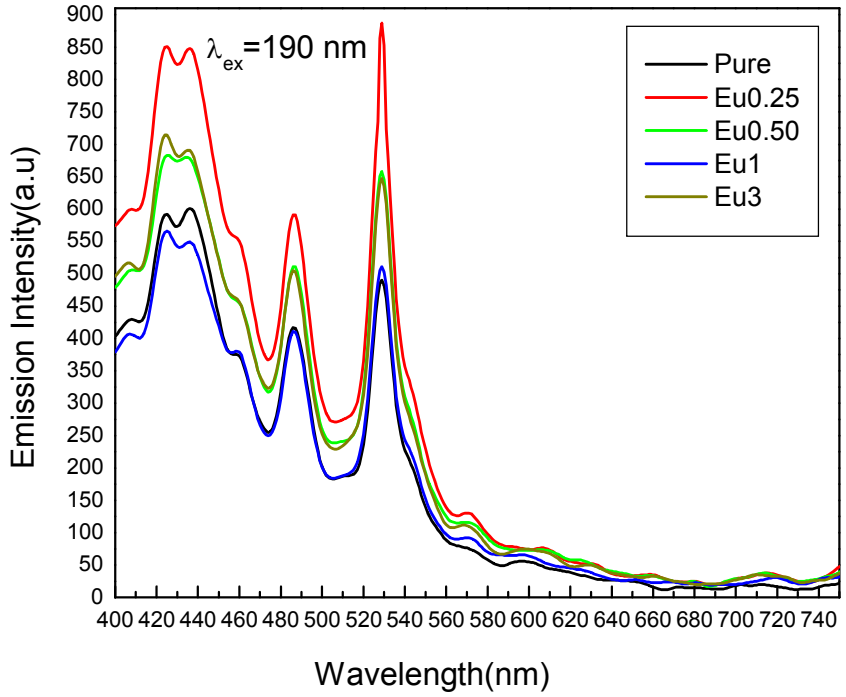

Fig.4.21 PL spectra of pure and Europium doped ZnO at λ_{ex}=190 nm.

From the above spectra it is quite clear that doping of Europium has no effect and at all concentrations of Europium, similar peaks as that of pure ZnO have been obtained. This happens because the excitation wavelength chosen is 190 nm which corresponds to energy of 6.52 eV, which is quite high. This sufficiently high energy excites the electrons from the deep levels of Zinc atoms and thus in the spectra the peaks obtained are mainly due to the Zinc atoms. Since Zinc atoms are more in number therefore, we can say that the peaks due to the impurity atoms get suppressed. In the spectra, the emission peaks obtained at 528 nm corresponds to emission of green color. This green color emission is attributed to the transition between singly charged oxygen vacancy and photo excited hole or Zn interstitial related defects in the ZnO. The peaks obtained at 486 nm correspond to blue color which is attributed to the transition of electron from the conduction band edge of ZnO to the valence

band edge i.e. corresponds to band gap transition. The peaks obtained below 450 nm lies in the ultraviolet region and are of no interest.

In order to investigate the effect of the excitation wavelength is changed in a regular passion and is shown in Fig.4.22.

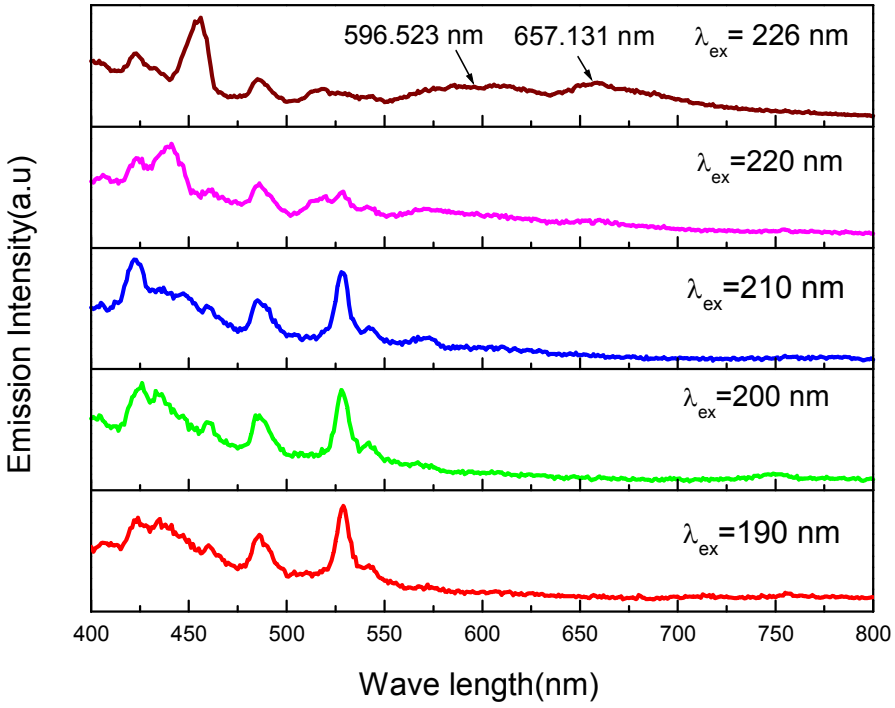

Fig.4.22 Effect of changing the excitation wavelength in ZnO: 0.25% Eu

The emission patterns reveals that as the excitation wavelength is increased (energy decrease) the peaks corresponding to the band gap transition and transition between singly charged oxygen vacancy and photo excited hole get suppressed with the appearance of new peaks. At an excitation wavelength of 226 nm two new broad peaks appeared at 596.523 nm and 657.131 nm corresponding to orange and red emission respectively. This inferring that at this wavelength (226 nm) the transitions from trapped levels generated by the doped atom taking place. Fig.4.23 shows the PL spectra obtained in ZnO: 0.25% Eu at 254 nm excitation wavelength.

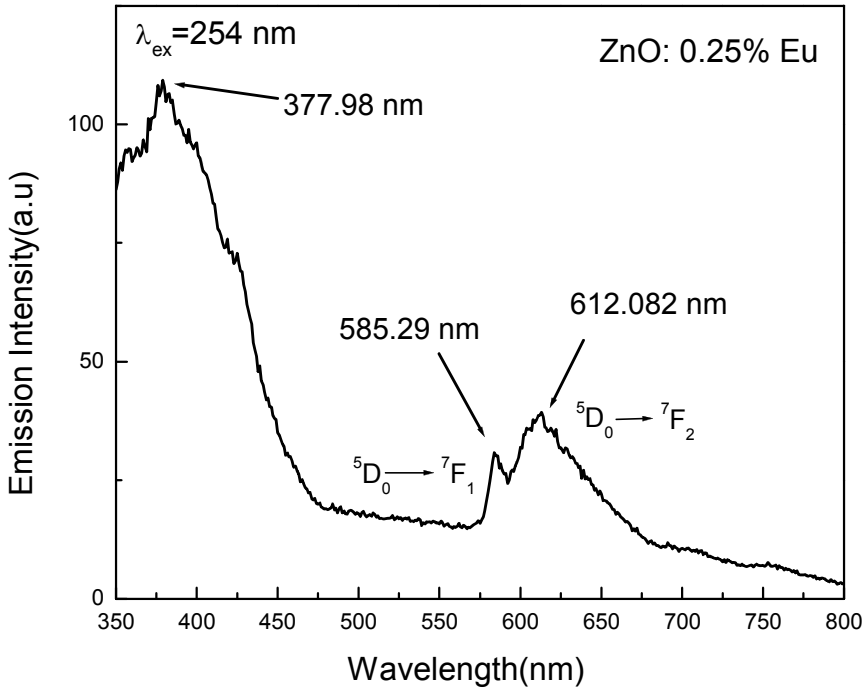

Fig.4.23 PL spectra of ZnO: 0.25% Eu at 254 nm excitation wavelength.

From the above spectra it is evident that at an excitation wavelength of 254 nm the peaks observed at 486 nm and 528 nm get disappeared and two new peaks at 585.29 nm and 612.082 nm were found. The disappearance of the peaks is attributed to the fact that at 254 nm the energy is not sufficient enough to photoexcite electrons of Zinc atoms. Since the added impurity creates a trapped level in the energy gap therefore at this wavelength the transition from the trapped levels occur. The peaks obtained at 585.29 nm and 612.082 nm are attributed to the characteristics emission of Eu^{3+}, corresponding to $^5D_0 \rightarrow {}^7F_1$, $^5D_0 \rightarrow {}^7F_2$ transitions respectively. The peak at 585.29 nm corresponds to yellow color while peak at 612.082 nm corresponds to orange color. The PL spectra of ZnO: 3% Eu has been shown in Fig.4.24. No significant changes have been observed with increase in the Europium concentration. Fig.4.24 represents the PL spectra of ZnO: 3 % Eu at 254 nm excitation wavelength.

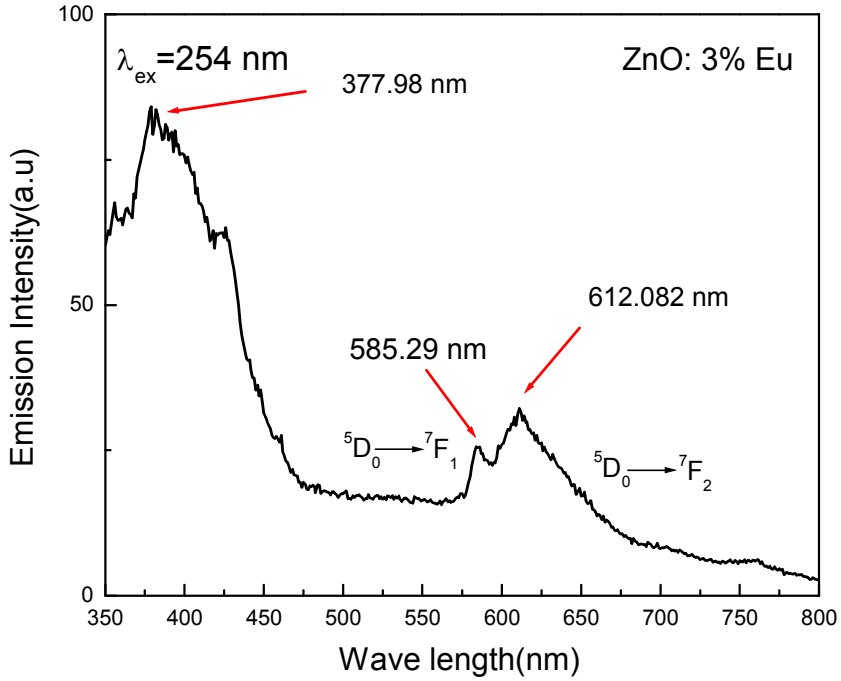

Fig.4.24 PL spectra of ZnO: 3 % Eu at 254 nm excitation wavelength.

In summary, we have observed luminescence of Europium doped ZnO due to intra -4*f* transitions of Eu^{3+} ions under low–energy excitation. The observed emission color is orangish-yellow. Moreover, at high-energy excitation greenish-blue color has been observed because of transition between singly charged oxygen vacancy and photo excited hole or Zn interstitial related defects in the ZnO. Thus, we can say the Europium doped ZnO is a promising material for optoelectronic device applications.

4.4) ANALYSIS OF DIELECTRIC AND FERROELECTIC PROPERTIES:

The dielectric and ferroelectric properties of pure and doped ZnO are investigated by using LCR meter (Agilent 4284 a precision LCR meter) and P-E loop tracer (Marine India automatic P-E loop tracer system). For this study, the powders of pure and doped ZnO prepared by co-precipitation method are taken and mixed with 0.2% PVA and then pressed in a 12.5 mm die to form pellets under 11 ton hydrostatic pressure. These pellets finally sintered at 900^0C for 2 hrs. It is noted that after sintering the pellets gets shrink. The percentage of shrinkage is calculated using

$$\% \text{ shrinkage} = \frac{\textit{Diameter of green body} - \textit{Diameter of sintered body}}{\textit{Diameter of green body}} \text{ X } 100$$

which is equal approximately equal to 12-14%. This large shrinkage attributed to the small crystallite size of the powders. After this, electroding on the pellets is done by using Silver paste for electronic measurements.

4.4.1) DIELECTRIC AND FERROELECTRIC PROPERTIES OF PURE ZnO:

Frequency dependent dielectric measurements of pure ZnO were measured at different frequencies (20 Hz ≤ f ≤ 1M Hz) from room temperature to 200^0c. Fig.4.25 shows the variation of dielectric constant as a function of frequency.

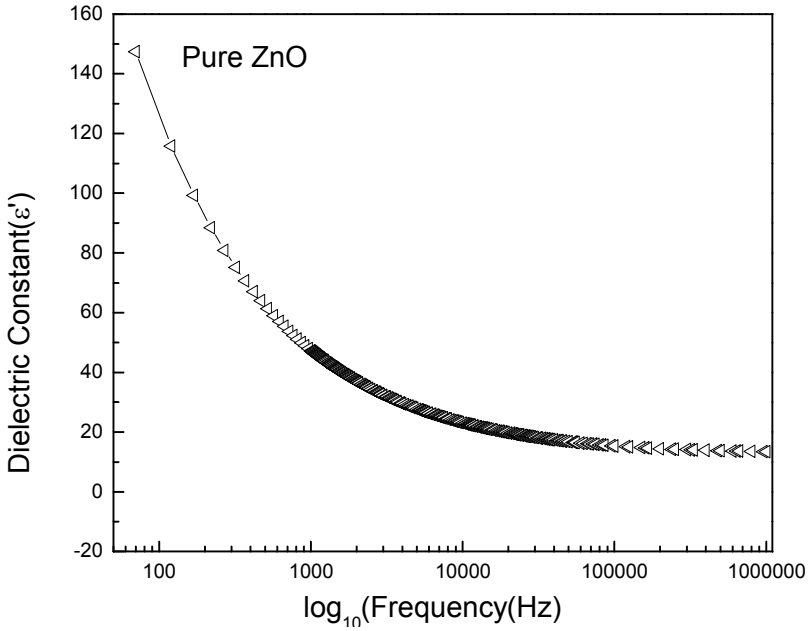

Fig.4.25 Variation of dielectric constant with the frequency (20 Hz ≤ f ≤ 1M Hz).

Temperature dependent variation of the real part of dielectric constant with temperature at different frequencies (20 Hz ≤ f ≤ 1M Hz) is shown in Fig.4.26.

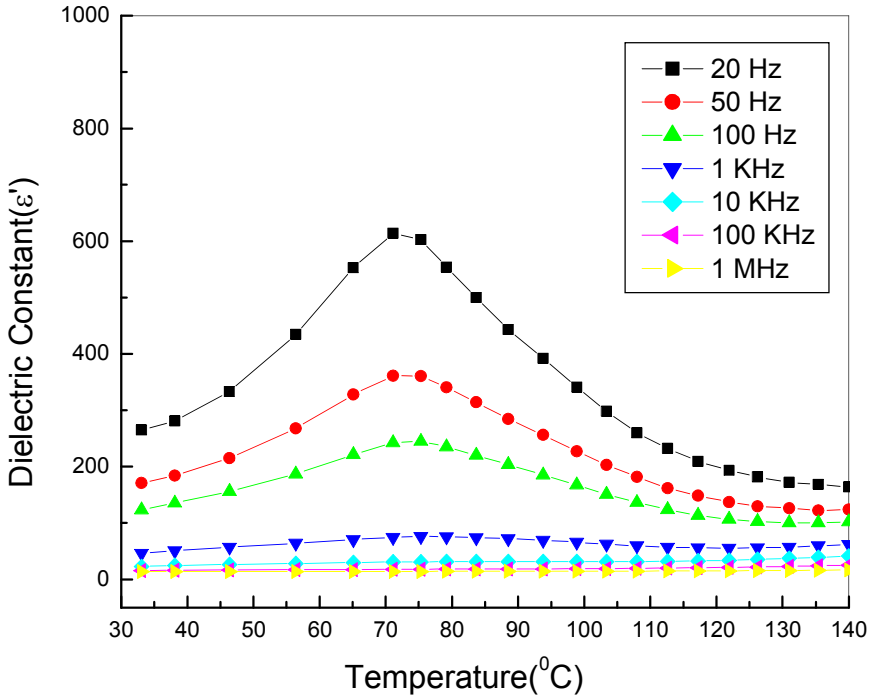

Fig.4.26 Variation of the dielectric constant with temperature at different frequencies

We observed that value of permittivity (ε') was minimum at lower temperature and gradually increase with increasing temperature to attain maxima at 71^0c, further increase in temperature lowers the value of permittivity (ε'), therefore sample shows a pure ferroelectric to paraelectric phase transition at 71^0c in all the frequency range (20 Hz ≤ f ≤ 1M Hz). The maximum value of the dielectric constant at T_c was observed to be 611 at 20 Hz frequency, which is quite large as compared to earlier reported values. This is attributed to the fact that the lattice parameters of the synthesized pure ZnO have greater value as compared to the commercial available ZnO as a consequence of which the ZnO lattice expands and thus the movement of Zn ion will be easier.

The variation of dielectric losses of the sample with the temperature has been shown in the Fig.4.27. We found that loss have maximum value at lower frequencies and lower temperature region, which further decrease with increase in the frequency and temperature

as well. However the magnitude is very low which significant point for the application point of view.

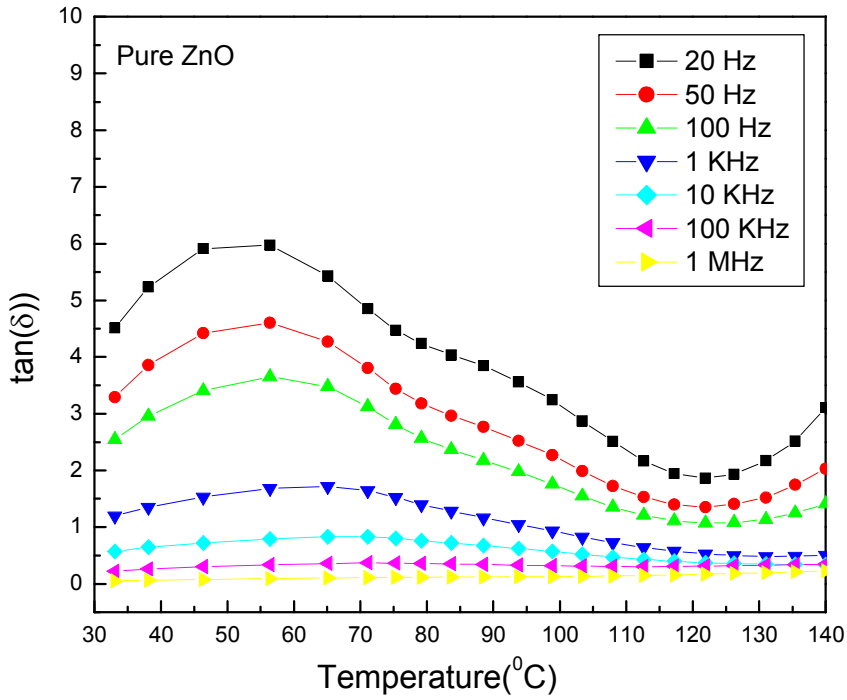

Fig.4.27 Variation of dielectric losses of the sample with temperature in pure ZnO

Further ferroelectric properties of ZnO were carried out using P-E loop tracer at room temperature in the (0-15 kV/cm) field.

Fig.4.28 demonstrates the P-E loop of the pure ZnO. It was found that the loop obtained was not a saturated one. This is attributed to the fact that the ferroelectric switching in case of ZnO is weak, though the hysteresis observed gives an idea of the existence of ferroelectricity in the sample. The remnant polarization (P_r) =5.44 μC/cm^2 and coercive field (E_c) = 10.37 KV/cm is obtained for the pure ZnO from the P-E hysteresis loop. Thus the presence of T_c in the dielectric constant (ε') vs. temperature profile and existence of hysteresis gives evidence for ferroelectricity in ZnO.

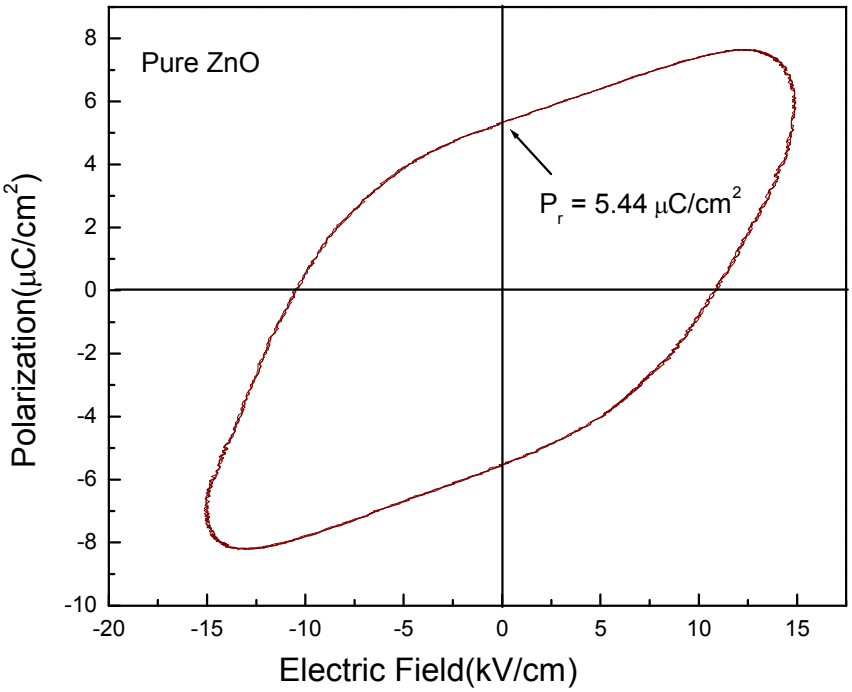

Fig.4.28 P-E loop of pure ZnO at room temperature

4.4.1) DIELECTRIC AND FERROELECTRIC PROPERTIES OF TITANIUM DOPED ZnO:

The doped ZnO samples were characterized by using LCR meter and P-E loop tracer to examine the dielectric and ferroelectric behavior. Titanium doping is expected to increase the polarization in the sample because of the greater charge on Ti i.e. +4 as compare to Zinc which is +2 and thus creates a mixed valency. This charge polarity and rotation of non-linear Ti-O bonds with respect to Zn-O bonds under electric field can give rise to ferroelectricity.

Dielectric properties of Titanium doped ZnO were measured at different frequencies (20 Hz $\leq$ f $\leq$ 1M Hz). Fig.4.29 represents the variation of the real part of dielectric constant as a function of frequency. From the figure it is evident that the value of dielectric constant decreased with the Titanium doping at 20 Hz frequency, which is 53 for ZnO: 0.25% Ti and 51 for ZnO:1% Ti. This is attributed to the fact that lattice constants of Titanium doped ZnO have smaller value as compared to the pure ZnO and therefore there is lattice contraction, which arises because the charge on Ti is +4 units and hence it attracts the oxygen anions towards itself with greater force as compare to Zn (which is + 2 units). Due

to these lattice contractions the lattice structure becomes more and more tightly packed. This tighter crystallographic geometry suppresses the relative displacement of Titanium ion, consequently the values of dielectric constant decreases.

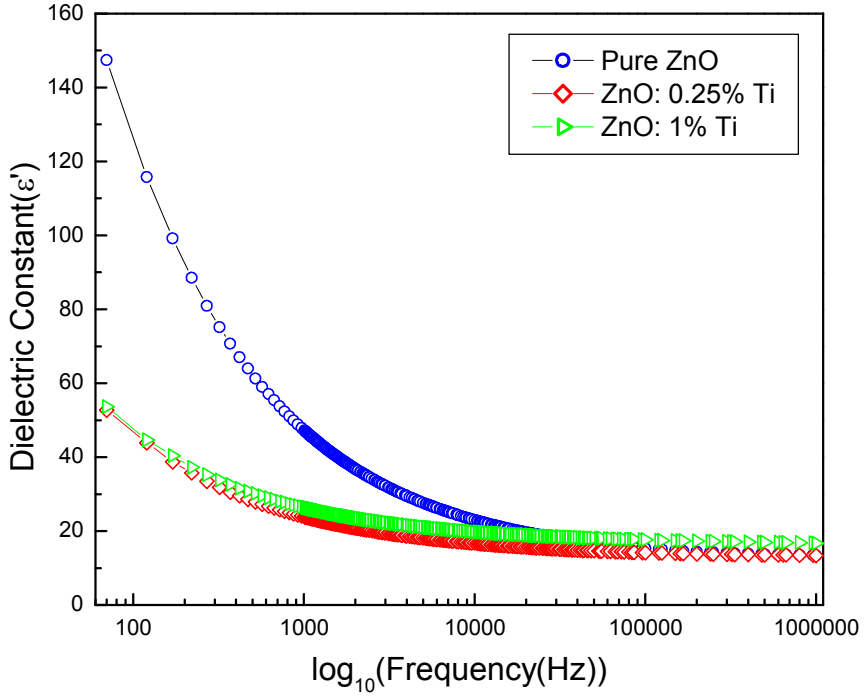

Fig.4.29 Variation of dielectric constant with frequency

Furthermore, with the increasing frequency the dielectric constant decreases in both 0.25%and 1% Titanium doped ZnO and become constant almost at higher frequency region, this is because at higher frequencies the dipoles are not been able to follow the field.

The variation of the real part of dielectric constant (ε') with temperature at different frequencies (20 Hz ≤ f ≤ 1M Hz) of 0.25% and 1% Titanium doped ZnO is shown in Fig.4.30a and Fig.4.30b. It was found that the addition of Titanium give rise to shift in T_C. The graphs reveals that the ferroelectric T_c observed in case of 0.25% Titanium doped ZnO is 82^0C, while the ferroelectric T_c of 1% Titanium doped ZnO is 157^0C suggesting that with the addition of Titanium in the ZnO ferroelectric T_c increases.

These shifts in the T_c were studied by Tai et al. [62] He reported the existence of microscopic scale polarization clusters in both the ferroelectric and the paraelectric phases in $BaTiO_3$, that is, the sample has spontaneously phase separated into polar clusters and non- polar

clusters which appear continuously across the Curie temperature T_c. When T_c is approached from above, particularly in the vicinity of Curie temperature there is a competition between the polar phase and the non polar phase. With the increase in the Titanium concentration the polar clusters grow in number at the expense of non polar clusters as a result of which the material enters into a ferroelectric state at higher temperature. Furthermore, peaks positions in both cases remain same at different frequencies indicting the absence of relaxation behavior. The maximum value of the dielectric constant at T_c for 0.25% Titanium doped ZnO comes out to be 145 at 20 Hz frequency, whereas the maximum value of the dielectric constant for 1% Titanium doped ZnO comes out to be 560 at 20 Hz. However, the magnitude of dielectric constant is lower than that of pure ZnO.

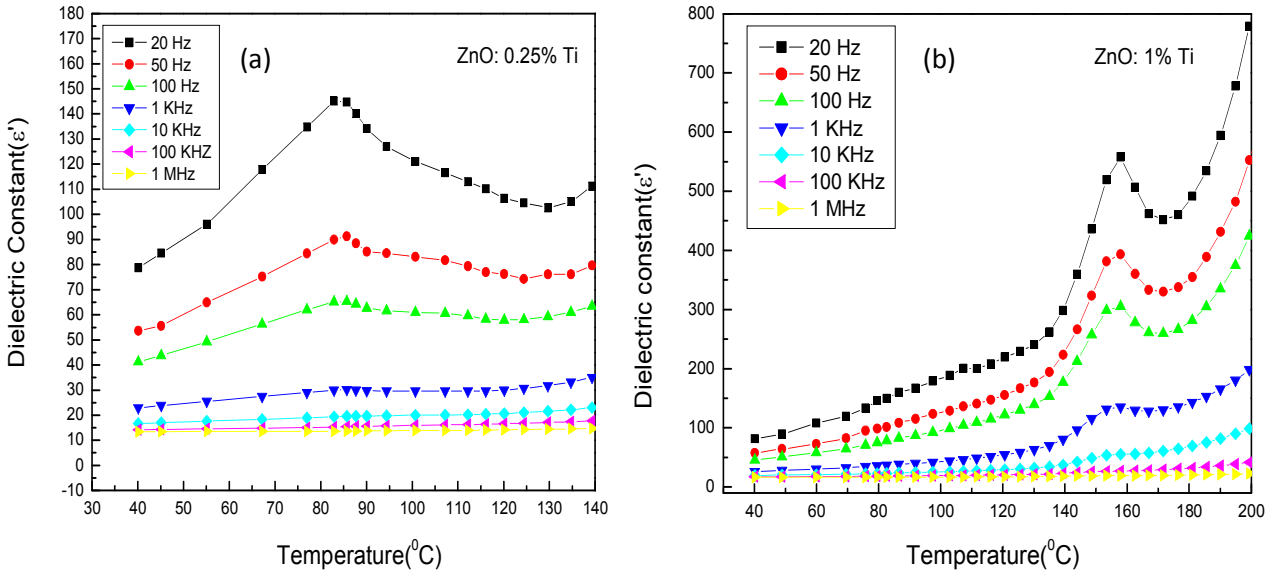

Fig.4.30 Variation of dielectric constant with temperature a) Ti=0.25% b) Ti =1%

Fig.4.31 shows the variation of Dielectric loss of 0.25% and 1% Titanium doped ZnO with temperature respectively. From the graph it can be conclude that the dielectric loss in the case of Titanium doped samples has been significantly reduced. However at high temperatures the loss has been increased at 1% Ti doped ZnO, this can be attributed to the fact that at high temperatures the conductivity of the semiconductors increases and as a consequence of which the losses increases.

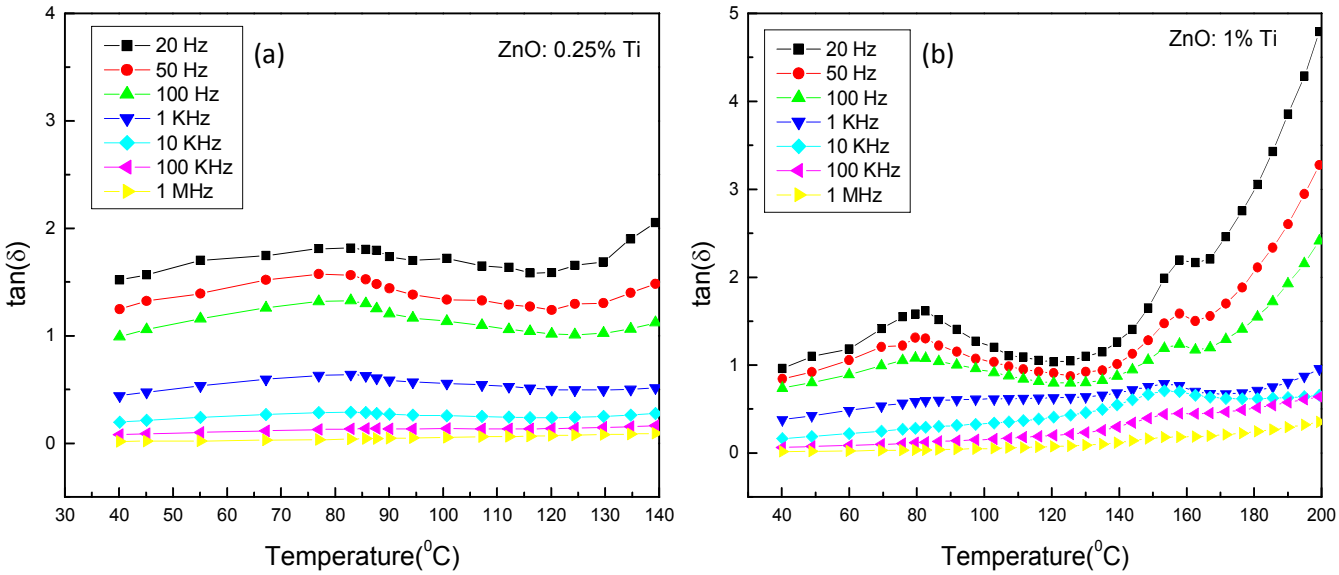

Fig.4.31 Variation of dielectric losses with temperature a) Ti=0.25% b) Ti =1%

For the further confirmation of ferroelectricity in Titanium doped ZnO P-E loops of the samples were measured using P-E loop tracer. Fig.4.32a and Fig.4.32b demonstrates the P-E loops of 0.25% and 1% Titanium doped ZnO respectively.

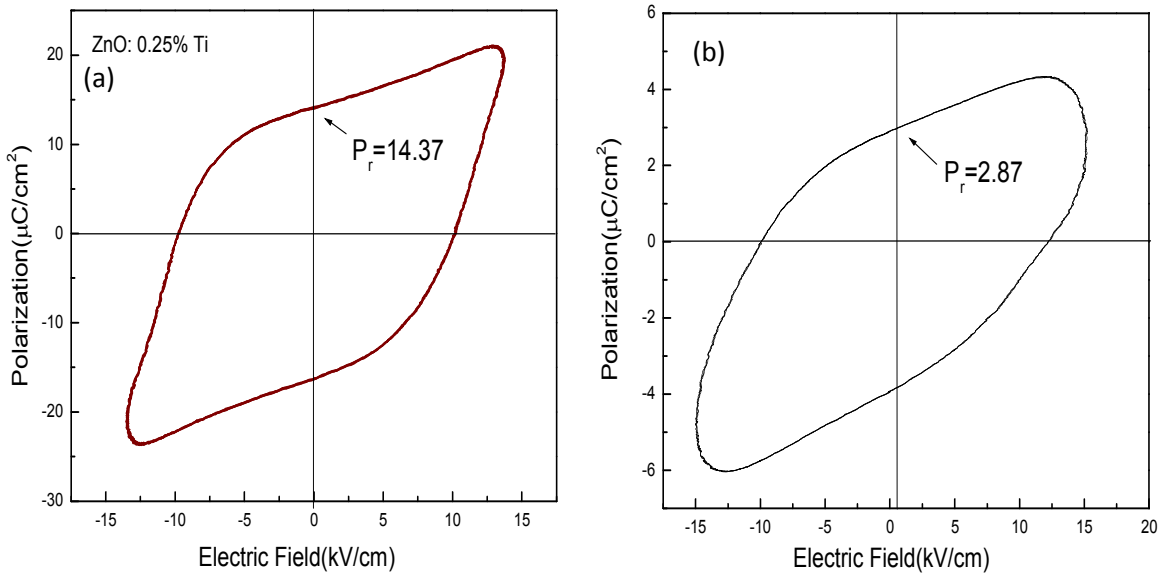

Fig.4.32 P-E loop of pure ZnO at room temperature a) Ti =0.25% b) Ti= 1%

The P-E loops observed for the samples shows hysteresis in Titanium doped ZnO, which gives an idea about the existence of the ferroelectricity in both sample. The P-E loop observed for 0.25% Titanium doped ZnO shows a little a bit saturation value (P_s) = 13.65

$\mu C/cm^2$ and the value of the remanent polarization has increased to a quite higher value (P_r) =14.37 $\mu C/cm^2$, which is close to that of Perovskite materials, whereas the loop obtained for 1% Titanium doped ZnO is highly unsaturated as a consequence of which the value of remnant polarization has decreased to (P_r) =2.87 $\mu C/cm^2$.

From the above analysis it can be concluded the pure ZnO and Ti doped ZnO exhibit ferroelectric properties which is being confirmed by the appearance of T_c in the dielectric vs. temperature profiles and hysteresis obtained in the P-E loop measurements. The doping of Titanium increases the ferroelectric T_c and remanent polarization which makes it a promising candidate for the technological applications.

4.5) MORPHOLOGICAL ANALYSIS OF PURE AND DOPED ZnO:

4.5.1) MORPHOLOGY ANALYSIS OF PURE ZnO:

The morphological analysis of the synthesized pure and doped ZnO has been done by using Scanning electron microscopy. Fig.4.33 shows the SEM image of synthesized pure ZnO.

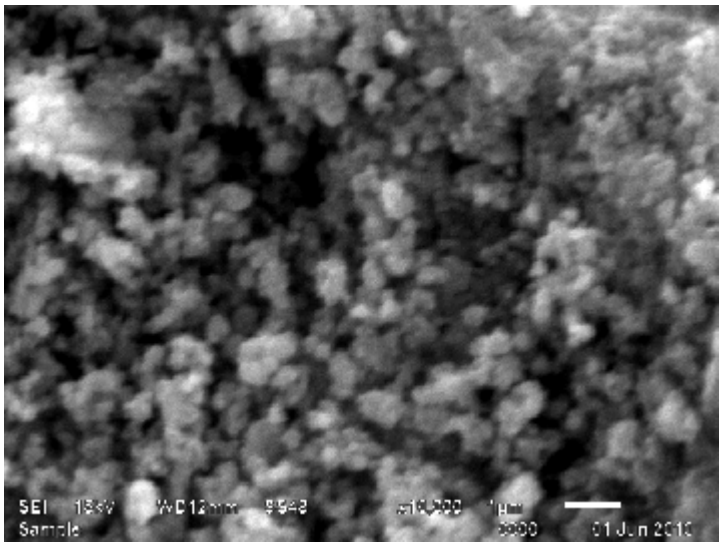

Fig.4.33 SEM image of synthesized pure ZnO

We found that no definite morphology has been obtained in the sample. But it is quite evident that the particles are visible and average particle is around 80-100 nm. To find out the exact particle size and distribution we need to characterize these samples by Transmission Electron Microscopy (TEM).

4.5.2) MORPHOLOGY ANALYSIS OF EUROPIUM DOPED ZnO:

Fig.4.34 display the SEM image of 0.25% Europium doped ZnO.

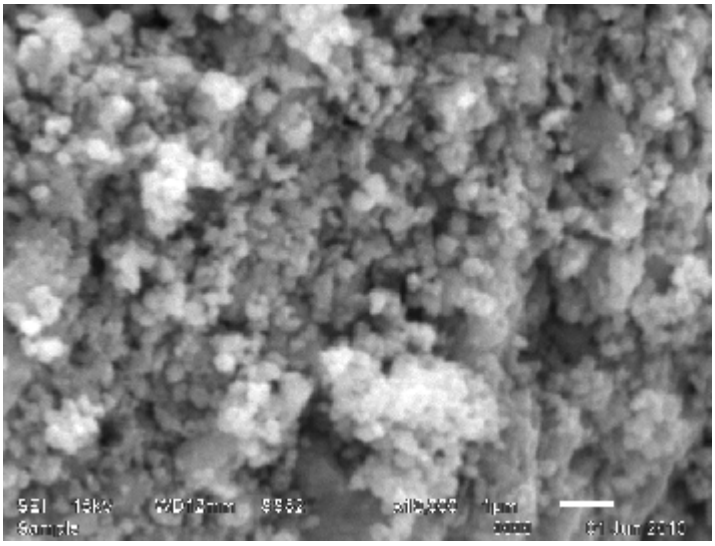

Fig.4.34 SEM image of synthesized 0.25% Europium doped ZnO

Same spherical crystallites were observed in this case, which seem to be agglomerate and form cluster. According to the scale (1μm) 10-12 crystallites in 1 μm gives an idea that size of crystallites is around 80-100 nm but still the exact information about the particle size will be govern by TEM analysis.

4.5.3) MORPHOLOGY ANALYSIS OF TITANIUM DOPED ZnO:

Fig.4.35 shows the SEM image of 0.25% Titanium doped ZnO. From the image it is clear that crystallite size is less than 1 μm with no definite morphology. It seems that the particles were agglomerated and form a cluster. As the particle size calculated from the XRD is in nano range we are not getting any exact information about the surface morphology of the sample from the SEM micrograph, due to the limitation of our instruments up to micro range.

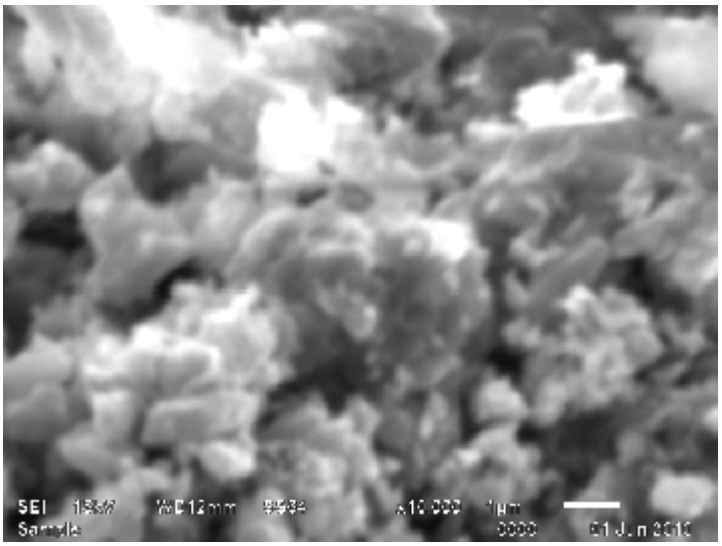

Fig.4.35 SEM image of 0.25% Titanium doped ZnO

The morphology observed in the sample not showing any hard grains which gives the idea that size of the particle is small and further needs to be characterized by Transmission electron microscopy (TEM) to obtained exact morphology and size of the particles.

CHAPTER 5

CONCLUSIONS AND FUTURE PRESPECTIVE

CONCLUSIONS:

- We have successfully synthesized pure and doped (Samarium, Europium, Titanium, and Niobium) ZnO exhibiting wurtzite hexagonal structure. The average particle size calculated by Scherer formula reveals that average particle size of pure ZnO was found 7 nm and increased with the doping of different materials. Also, change in the lattice constants and absence of extra peaks in XRD gives information about the successful doping which enhances the physical properties.
- Chemical analysis also supporting the XRD analysis as it gives only Zn-O reflection.
- From the optical analysis we conclude that with addition of dopant the exciton peak gets shifted to higher wavelength which reveals the formation of impurity states inside the forbidden gap, thus decrease the band gap.
- The emission spectra obtained for pure and doped ZnO reveals the presence of phosphorescence. Green and blue emissions was found consistence in pure and doped samples. However, the rare earth elements doped ZnO gives orange and yellow emission, which can be used in many technological applications.
- From SEM images it is clear that no definite morphology has been observed. It seems that particles are agglomerated and form clusters. In order to determine the definite morphology and particles size distribution samples need to be characterized by Transmission Electron Microscopy.
- Appearance of transition temperature T_c (71^0c) in pure ZnO, (82^0c) in 0.25% Ti doped ZnO and (157^0c) in 1% Ti doped ZnO infer about the presence of ferroelectricity in pure as well as Titanium doped ZnO, which is further verified by hysteresis observed in P-E loops.

FUTURE PRESPECTIVE:

Phosphor and Ferroelectric materials serves as useful and important part in devices. These materials are known for their low price, high sensitivity and low voltages operations. The number of applications expanded steadily during the next three decades and is now entering an age of integration and miniaturization in which three-dimensional ceramic circuitry is being developed. Further advances will undoubtedly occur in the years ahead as the field electroceramics follows in the footsteps of the semiconductor industry which will lead to production of MEMS devices in which both electronics and the mechanical components are joined together. Furthermore, nanophosphors are the promising candidates for the electro-optic devices.

REFERENCES:

1) R. Rossetti, R. Hull, J.M. Gibson and L.E. Brus, J. Chem.Phys. **552**, 82 (1985).
2) L.E. Brus, J.Phys. Chem. **2555**, 90 (1986).
3) A. Henglein, Chem. Rev. **1861**, 89 *(*1989).
4) Y Wang and N. Herron, J.Phys.Chem. **525,** 95 (1991).
5) S.H.Huang, H. K. Shang, X. Y. Teng, Y. S. Wang, Z. G.Yao and X. Q. Zhang, Chin. Phys. **14,** 1205 (2005)
6) S. Y. Lee, E. S. Shim, H. S. Kang, S. S. Pang and J. S. Kang, Thin Solid Films **437,** 31 (2005)
7) R. Konenkamp, R. C. Word and C. Schlegel, Appl.Phys. Lett. **85,** 6004(2004)
8) H. T. Ng, J.Han , T. Yamada, P. Nguyen, Y. P. Chen and M. Meyyappan, Nano lett. 4, 1247 (2004).
9) Z. L. Wang, Adv. Mater. **19,** 889 (2007).
10) M. H. Huang, S. Mao, H. Feick, H. Q. Yan, Y. Y. Wu, H. Kind, E. Weber, R. Russo and P.D. Yang, Science **292,** 1897 (2001).
11) S. Baruah and J. Dutta, Sci. Technol. Adv. Mater. **10**, 013001 (2009).
12) A. Hernandezbattez, R.Gonzalez, J. Viesca, J.Fernandez, J. Diazfernandez, A. Machado, R. Chou, and J. Reba,Wear **265**, 422 (2008).
13) U. Ozgur, Y.I. Alivov, C. Liu, A. Teke, M. A. Reshchikov, S.Dogan, V. Avrutin and S. Cho, Journal of Applied Physics **98**, 041301 (2005).
14) http://www.lamptech.co.uk/Documents/FL%20Phosphors.html
15) D. Brewster, J. Sci. **1**, 208 (1824).
16) J.Curie, and P. Curie, Bull. Soc. Min de France **3**, 90 (1880).
17) H. Mueller, Fhs**.** Rev. **47**, 175 (1935).
18) H. Mueller, Jhs. Rev. **57,** 829(1940).
19) H. Mueller, Fhys. Rev. **58**, 565(1940).
20) H. Mueller, Fhys. Rev. **58**, 8051 (1940).
21) G. Busch and P. Scherer, Naturwiss **23**, 737 (1935)**.**
22) J. West, Z. Krrst. **74**, 306 (1955).
23) B. Jaffe, R. S. Roth, and l. Marzullo, J. Appl. fhys. **25**, 804 (1955).
24) B. Jaffe, R. S. Roth, and S. Marzullo, J. Res. Nag. Bur. Stand. **55** 239(1955).

25) http://www.answers.com/topic/phosphorescence
26) P. Elumalai, P. Atkins and Paula, J. Atkins Physical Chemistry, Oxford University Press, 2002. ISBN 0-19-879285-9.
27) http://micro.magnet.fsu.edu/primer/java/jablonski/lightandcolor
28) D . Look, Materials Science and Engineering B **80**, 383 (2001).
29) D.Heiman, "Photoluminescence spectroscopy" Physics U600 Adv lab I-Physics of waves and optics Northeastern University (2004).
30) K.L. Choy, A. L. Heyes and J. Feist, U.S. Patent 6,974,641 (1998).
31) A. M. Srivastava, A. A. Setlur, H. A. Comanzo, J. W. Devitt, J. A. Ruud and L. N. Brewer, U.S. Patent 6,730,918B2 (2001).
32) J. P. Feist and A. L. Heyes, GB. Patent 0318929.7 (2003).
33) Z.L. Wang, J. Phys. Condens. Matter. **16**, 829 (2004).
34) D.O. Boatner and Diebold, Surf. Sci. **519**, 201 (2002).
35) B. Mayer and D. Marx, Phys. Rev. B **67**, 035403 (2003).
36) O. Dulub, U. Diebold and G. Kresse, Phys. Rev. Lett. **90**, 016102. (2003)
37) A. Wander, F. Schedin, P. Steadman, A. Norris, R. Mcgrath, T.S. Turner, G. Thorton and N.M.Harrison, Phys. Rev. Lett. **86**, 3811 (2001).
38) V. Staemmler, K. Fink, B. Mayer, D.Marx, M. Kunat, U.Burghaus,and Woll, Phys.Rev. let. **90**, 106102 (2oo3).
39) Y.C.Yang, C.Song,X.H. Wang, F. Zeng and F.Pan, App. Phys. Lett. **92**,012907 (2008).
40) C. H. Henry, K. Nassau, and J. W. Shiever, Phys. Rev. B **4**, 2453 (1971) .
41) B.J. Pierce and R.L. Hengehold, J. Appl. Phys. **47**, 644 (1976).
42) M. Liu, A. H. Kitai and P. Mascher, J. Luminescence **54,** 35 (1992).
43) Y.Hayashi, H. Narahara, T. Uchida and T. Noguchi, Jpn. J.Appl.Phys. **34,** 1878 (1995).
44) J. Zhong, A.H. Kitai and P. Mascher, J. Electrochem. Soc. **140**, 3644 (1993).
45) K. Vanheusden, W.L. Warren, C.H. Seager, D.R. Tallant, J. A. Voigt and B.E. Gnade, J. Appl. Phys **79**, 7983 (1996).
46) S.A. Studenikin, Nikolay Golego and Michael Cocivera, J. Appl. Phys **84**,2287 (1998).
47) A.A.Bol and A.Meijerink, Phys. Rev. B **58**, 15997 (1998).
48) A.Ishizumi and Y. Kanemitsu, Appl. Phys. Lett. **86**, 253106 (2005).
49) Y. Wang and B. Chu, Supperlattices and Microstructures **44**,54-61(2008).

50) P. Kumbhakar, D.Singh, C.S. Tiwary and A.K. Mitra, Chalcogenide letters **5**, 387 (2008).

51) Li Chen, Jiahua Zhang,,Xianmin Zhang, Feng Liu and Xiaojun Wang , Optics Express **16**, 11795 (2008).

52) Zhang Fu-Chun, Zhang Zhi Yong, Zhang Wei-Hu, Yan Jun-Feng and Yong Jiang-Ni, Chinese Physics B **18**, 2506 (2009).

53) Dongqi Yu, Lizhong Hu, Shuangshuang Qiao, Heqiu Zhang, Song-En Andy Len, L K Len, Qiang Fu, Xi Chen and Kaitong Sun, J. Phys. D: Appl. Phys. **42**, 055110 (2009).

54) A. Onodera, N. Tamaki, K. Yoshio, H. Satoh, T. Takama and H. Yamashita, IEEE Xplore **8**, 475 (1998).

55) M. Joseph, H.Tabata and T. Kawai, Appl. Phys. Lett. **74**, 2534 (1999).

56) Zhao M H, Wang Z L and Mao S X, Nano *Lett.* **4**, 587 (2004).

57) M. Alexe, D. Hesse, V. Schmidt, S. Senz, H. J. Fan, M. Zacharias, and U. Gosele, App. Phys. Lett. **89**, 172907 (2006)

58) Dhananjay and J. Nagaraju, J. App. Phy. **99**, 034105 (2006).

59) Y. C. Yang, C.Song , X. H. Wang, F. Zeng and F. Pan, Appl.Phys. Lett. **92**, 012907 (2008)

60) Y.Q. Chen, X. J. Zheng and X. Feng, Nanotechnology **21,** 055708 (2010).

61) C.W. Zou, H.J. Wang, M.L. Yin, M. Li, C.S. Liu, L.P. Guo and D.J. Fu, Journal of Crystal Growth **312**, 906 (2010).

62) R. Z. Tai *et al.*, Phys. Rev. Lett. **93**, 087601 (2004).